Aeroacoustic Analysis of a Closely Installed Chevron Nozzle Jet using the High-Order Discontinuous Galerkin Method

Daniel Lindblad[*], Spencer J. Sherwin[†] and Chris D. Cantwell [‡]
Imperial College London, London, SW7 2AZ, United Kingdom

Jack L.T. Lawrence[§]
University of Southampton, Southampton, SO17 1BJ, United Kingdom

Anderson R. Proença[¶]
Cranfield University, Cranfield, MK43 0AL, United Kingdom

Margarida Moragues Ginard[‖]
Basque Center for Applied Mathematics, Bilbao, 48009, Spain

In this paper, we use Large Eddy Simulations (LES) in combination with the Ffowcs Williams - Hawkings method to study the influence of chevrons on the flow field as well as the noise produced by a closely installed M = 0.6 jet. The LES simulations are performed with the spectral/hp element framework Nektar++ (www.nektar.info). Nektar++ uses the high-order discontinuous Galerkin method and an implicit scheme based on the matrix-free Newton-GMRES method to discretize the unfiltered Navier-Stokes equations in space and time, respectively. The far-field noise is computed using Antares (www.cerfacs.fr/antares/). Antares solves the Ffowcs Williams - Hawkings equation for a permeable integration surface in the time-domain using a source-time dominant algorithm. The aerodynamic results show good agreement with experimental data obtained in the Doak Laboratory Flight Jet Rig, located at the University of Southampton. Some discrepancies are observed in terms of the far-field noise levels, especially for higher polar observer angles relative to the downstream jet axis. In terms of noise reduction potential, the simulations predict that the chevrons reduce the OASPL by 1dB compared to an installed round nozzle for all observers located on the unshielded side of the wing. This should be compared to the experiments, which predict a 1.5dB noise reduction for the same chevron nozzle.

I. Nomenclature

Roman/Greek

c = speed of sound, m s^{-1}
D_j = diameter of nozzle, m
f = frequency, s^{-1}
H = vertical distance between center of nozzle exit and wing trailing edge, m
L = axial distance between center of nozzle exit and wing trailing edge, m
M_a = acoustic Mach number
p = pressure, kg m^{-1} s^{-2}
P = polynomial degree
r = distance between microphone and nozzle exit, m
t = time, s

---

[*]Research Associate, Department of Aeronautics, South Kensington Campus, London SW7 2AZ.
[†]Professor, Department of Aeronautics, South Kensington Campus, London SW7 2AZ.
[‡]Senior Lecturer, Department of Aeronautics, South Kensington Campus, London SW7 2AZ.
[§]Senior Research Fellow, Institute of Sound and Vibration Research, Highfield, Southampton SO17 1BJ, Member AIAA.
[¶]Lecturer in Aerodynamics, School of Aerospace, Transport and Manufacturing, Cranfield, MK43 0AL, Member AIAA.
[‖]Marie Skłodowska-Curie Action-IF Researcher, Computational Mathematics, Alameda de Mazarredo 14, 48009 Bilbao.

T	=	temperature, K
u_i	=	Cartesian velocity component, m s^{-1}
U_j	=	velocity at nozzle exit, m s^{-1}
x_i	=	Cartesian coordinate, m
γ	=	ratio of specific heats
θ	=	observer angle
μ	=	dynamic viscosity, kg m^{-1} s^{-1}
ρ	=	density, kg m^{-3}
τ	=	sampling interval, s

Subscripts/Superscripts

| $\square_\infty$ | = | far-field value |
| $\square^*$ | = | non-dimensional quantity |

Abbreviations

DG	=	discontinuous Galerkin
DOF	=	degrees of freedom in DG discretization
OASPL	=	overall sound pressure level
PSD	=	power spectral density
RMS	=	root mean square

II. Introduction

JET noise has been one of the dominant sources of aircraft noise during take-off for over half a century. This has motivated substantial research on the topic, starting with the first golden age of aeroacoustics in the middle of the last century [1]. An important result that came out of this work is that jet noise scales with the eighth power of the jet velocity [2, 3], whereas the propulsive power only scales with the third power of the jet velocity [1]. As a result, it is possible to reduce jet noise and maintain thrust by reducing the velocity and increasing the diameter of the jet. To achieve this, high-bypass ratio turbofan engines are used. Since a lower jet velocity also increases the propulsive efficiency of the engine, new turbofan engines with even higher bypass ratios will likely be introduced in the future.

Larger engines must be installed closer to the wing in order to maintain sufficient ground clearance. This inevitably leads to stronger interaction between the jet and the wing. In particular, it has been found that the hydrodynamic pressure field generated by the jet will be scattered by the trailing edge of the wing [4], which in turn leads to additional low-frequency noise with a dipole-like polar directivity. In addition to this, the high-frequency noise decreases above the wing and increases below the wing as a result of shielding [4–6].

To address the additional noise produced by installed jets, and thereby enable the use of efficient ultra high bypass ratio turbofan engines, several noise reduction technologies (NRTs) have been developed. These include, but are not limited to, porous trailing edges [7, 8], swept trailing edges [9], active flow control [10], and chevron nozzles [11]. Of these, the chevron nozzle is perhaps the most mature, given that it is currently in active service on a number of commercial aircraft. For an excellent overview of the development of chevron nozzles, the interested reader is referred to [11].

The purpose of this paper is to assess the influence of chevrons on the flow field and noise produced by a closely installed jet. To this end, a recently developed computational framework for jet noise [12, 13] based on the spectral/hp element framework Nektar++ [14, 15] and the Antares library [16–18] is used. In particular, the compressible flow solver implemented in Nektar++ is used to solve the unfiltered Navier-Stokes equations on unstructured grids using the high-order discontinuous Galerkin (DG) method [19, 20] in combination with implicit time stepping [21, 22]. The solution obtained with Nektar++ is then coupled with Antares to compute the far-field noise. Antares solves the Ffowcs Williams - Hawkings equation [23] for a porous integration surface [24] in the time domain using a source time dominant algorithm.

An important advantage of the DG method is that it can reach a high order of accuracy on unstructured grids. This makes it an interesting candidate for computational aeroacoustics, where low dissipation and dispersion errors are of paramount importance. Despite this, relatively few studies to date have used the DG method, or similar high-order

methods, such as the flux reconstruction method [25], to study jet noise, see e.g. [12, 13, 26, 27]. Instead, finite volume and finite difference methods are predominantly used, see e.g. [28–41] and [42–47]. Together with several review papers [48–50], these studies demonstrate the tremendous progress that has been made in numerical jet noise predictions based on scale resolving simulations over the past decades.

In order to reach the same level of maturity for numerical jet noise predictions as finite volume and finite difference methods, more research into the strengths and weaknesses of the DG method (and similar high-order methods) is needed. To this end, the simulations presented in this paper are compared against high-quality experimental data obtained in the Doak Laboratory Flight Jet Rig, located at the University of Southampton [51]. In general, the simulations are found to predict aerodynamic quantities in the jet quite well. The noise reduction potential of the installed chevron nozzle is also captured accurately. In terms of absolute noise levels, however, some discrepancies are observed, especially for the highest and the lowest frequencies.

III. Case Description

In this work, we consider a single stream nozzle with an inner diameter of $D_j = 40$ mm, a convergence half-angle of $2.44°$, and a total length of $19D_j$. Two variants of this nozzle are considered, a round nozzle without any noise reduction technology, and a serrated nozzle with 16 chevrons that are distributed uniformly around the circumference. In the latter case, each chevron has a flow penetration angle of $9°$. The round nozzle is considered both in an isolated and an installed configuration, whereas the chevron nozzle is only considered in an installed configuration. In the installed configuration, the nozzle is placed under a NACA4415 airfoil at $4°$ angle of attack. The span and length of the airfoil are equal to $3.75D_j$ and $15D_j$, respectively. The axial and vertical distance between the nozzle exit and the airfoil trailing are equal to $L = 3D_j$ and $H = 0.6D_j$, respectively. A schematic view of the installed chevron nozzle is shown in Fig. 1.
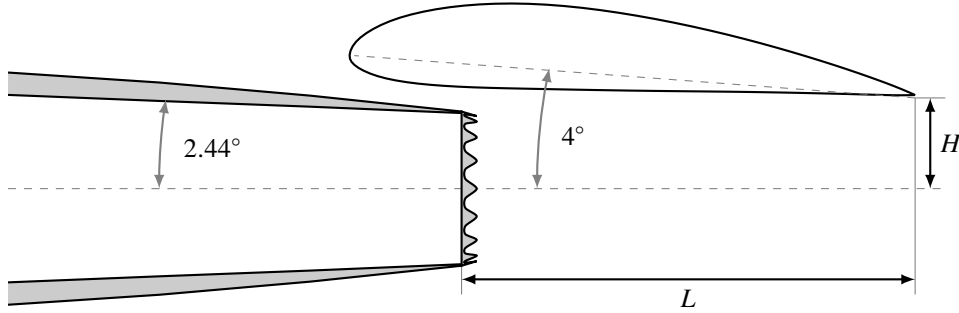

Fig. 1   Schematic view of the chevron nozzle installed under the wing.

All nozzles considered in this work operate at an acoustic Mach number of $M_a = U_j/c_\infty = 0.6$, a Reynolds number of $Re_j = \rho_\infty U_j D_j/\mu_\infty = 5.5 \cdot 10^5$, and a static temperature ratio of $T_j/T_\infty = 0.9335$. No flight stream is considered in this work.

IV. Numerical Method

This section gives a brief overview of the numerical method used to compute the far-field noise. The computation is split into two parts. In the first part, the turbulent jet is simulated using Nektar++. The solution obtained with Nektar++ is then exported to Antares, which uses the Ffowcs Williams - Hawkings method to compute the far-field noise. More details on the numerical method can be found in [12, 13].

A. Flow Solver

The compressible flow solver implemented in the spectral/hp element framework Nektar++ solves the Navier-Stokes equations in coupled, conservative form using the high-order discontinuous Galerkin (DG) method [14, 15, 21, 22, 52]. In the DG method, the solution in each mesh element is approximated by a basis of high-order polynomials up to degree P. To solve for the polynomial coefficients, a standard Galerkin projection of the governing equations onto the underlying polynomial basis is performed. For each mesh element, the advection terms are then integrated by parts in order to obtain a new volume integral, plus a surface integral over the element boundaries. Since the solution is not

required to be continuous across element boundaries in the DG method, Roe's [53] approximate Riemann solver is used to obtain a unique solution on each element boundary. This solution is then used to compute the surface integral, which represents the advective flux across the element boundaries. The diffusive terms are treated with the Interior Penalty (IP) method. More details about the implementation of the Riemann solver can be found in [21, 52]. The implementation of the IP method is described in [22].

The discrete equations obtained from the spatial discretization are integrated in time using a second-order, singly diagonally implicit Runge-Kutta method. The nonlinear system obtained from the temporal discretization is solved using a preconditioned, matrix-free Newton-GMRES algorithm [54], see [22] for details.

In this work, we solve the unfiltered Navier-Stokes equations. This implies that we rely on the numerical dissipation introduced by the discretization to model the transfer of energy between the resolved and the unresolved scales. Previous work has shown that the DG method in combination with Roe's approximate Riemann solver is well suited for this purpose [55–61].

Following [31], we non-dimensionalize the Navier-Stokes equations using the diameter of the nozzle, the density in the far-field, the speed of sound in the far-field, and the temperature in the far-field. This leads to the following non-dimensional quantities

$$\rho^* = \frac{\rho}{\rho_\infty}, \quad u_i^* = \frac{u_i}{c_\infty}, \quad p^* = \frac{p}{\rho_\infty c_\infty^2} = \frac{p}{\gamma p_\infty}, \quad T^* = \frac{T}{T_\infty}, \quad t^* = \frac{tc_\infty}{D_j}, \quad x_i^* = \frac{x_i}{D_j}. \tag{1}$$

Here, $\square^*$ denotes a non-dimensional quantity, $\square_\infty$ denotes a far-field value, $\gamma = 1.4$ is the ratio of specific heats, and D_j is the diameter of the nozzle. In this work, we assume that the gas is calorically perfect and obeys the ideal gas law. Since the nozzle is close to isothermal, we also assume that the viscosity is constant and equal to the far-field value.

B. Far-field Noise Prediction

The far-field noise is computed using Antares [16–18]. Antares solves the Ffowcs Williams - Hawkings equation [23] for a permeable integration surface [24] in the time domain using a source-time dominant algorithm. At present, Antares provides two solution formulations: Formulation 1A by Farassat [62] (for cases without a flight stream); and Formulation 1C by Najafi-Yazidi et al. [63] (for cases with a flight stream). Since no flight stream is considered in this work, Formulation 1A is used.

The contribution from the volume integral in the solution to the Ffowcs Williams - Hawkings equation is commonly omitted in LES studies of jet noise [49, 64, 65]. This simplification is valid as long as the integration surface encloses all relevant noise sources [24] and no significant entropy or vorticity waves cross the integration surface [28, 64]. In LES computations of turbulent jets, the latter condition is typically hard to satisfy at the downstream end of the integration surface [28, 64]. As a result, spurious noise is generated when entropy and/or vorticity waves cross the integration surface. Several solutions to this problem have been proposed in the literature, including the method of end-caps [28], the pressure formulation of the Ffowcs Williams - Hawkings equation [64], and the additional surface terms proposed by Rahier et al. [66]. Alternatively, the integration surface can be left open at the downstream end [26, 35, 38, 40, 67]. The last option can lead to poor predictions of the lowest frequencies [28, 65]. Therefore, the method of end-caps [28], possibly in combination with the pressure formulation of the Ffowcs Williams - Hawkings equation, or the additional surface terms proposed by Rahier et al. [66] are often preferred. However, for the sake of simplicity, an open end-cap was chosen for the simulations performed in this work. In addition to this, the pressure formulation was not used since it did not give any advantage for the cold jets considered in this work [12].

Antares is used to compute the non-dimensional pressure signal at the same microphone locations as in the experiments, see Fig. 2. After this, the power spectral density (PSD) is computed from the non-dimensional pressure signal using the implementation of Welch's method [68] available in SciPy v1.2.1 [69]. In this work, we use a 50% overlap and a Hann window function for Welch's method. For the isolated jet, we also average the PSD over 36 microphones placed uniformly around the circumference. This is done to compensate for the relatively short time signal obtained from the simulations. More details on how the PSD is computed can be found in [12].

The PSD obtained from the above procedure is non-dimensional. In order to compare with experiments, we scale the PSD using the ambient conditions measured in the experiments. More precisely, we compute the PSD in $[dB/St]$ as

$$\text{PSD}(St) = 10 \log_{10} \left(\frac{(\gamma p_\infty)^2 M_a \hat{P}^*(St M_a)}{p_{\text{ref}}^2} \right) + 20 \log_{10} \left(\frac{r}{r_{\text{ref}}} \right). \tag{2}$$

Here, $St = fD_j/U_j$ is the Strouhal number, $M_a = U_j/c_\infty$ is the acoustic Mach number, $\hat{P}^*(f^*)$ is the non-dimensional PSD, and $p_{\text{ref}} = 20 \cdot 10^{-6}$ Pa is the reference pressure. To stay consistent with the post-processing procedure used for the experimental data, we also scale the PSD to $r_{\text{ref}} = 1$m distance by adding $20\log_{10}(r/r_{\text{ref}})$, where r is the distance between the microphone and the nozzle exit (in meters).

The Overall Sound Pressure Level (OASPL) can be computed by either integrating the PSD over a chosen frequency band, or by computing the RMS of the pressure in the far field. In the latter case, the contribution from all frequencies is included in the OASPL. In this work, we chose the latter option, and compute the OASPL in [dB] as

$$\text{OASPL}(St) = 20\log_{10}\left(\frac{\gamma p_\infty p^*_{\text{rms}}}{p_{\text{ref}}}\right) + 20\log_{10}\left(\frac{r}{r_{\text{ref}}}\right). \tag{3}$$

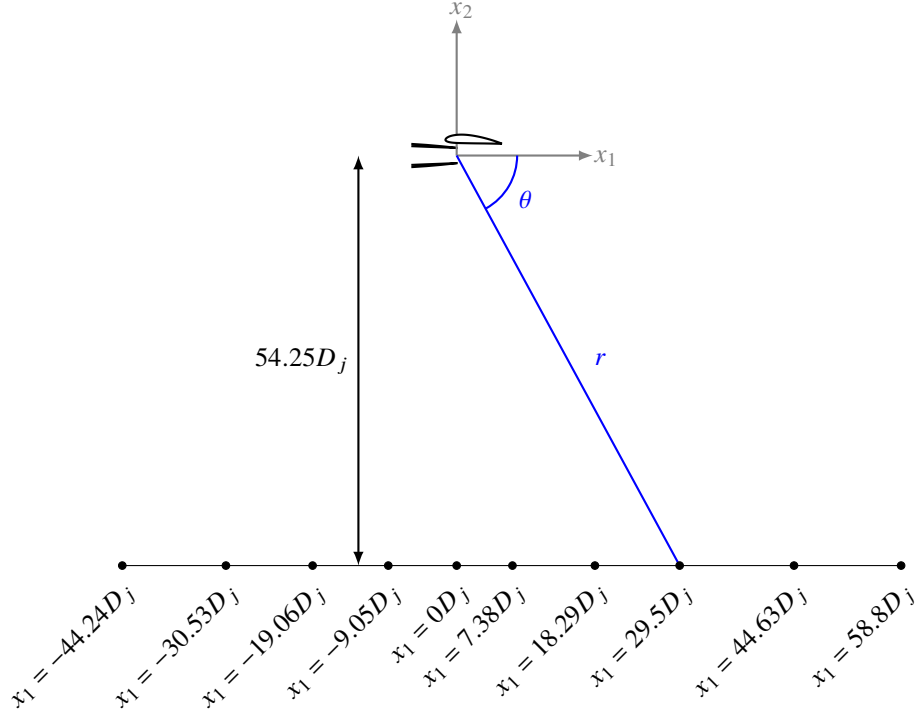As for the PSD, the OASPL is scaled to $r_{\text{ref}} = 1$m distance.

Fig. 2   Schematic view of the far-field microphone locations and the definition of the observer angle.

C. Computational Setup

1. Computational Domain and Boundary Conditions

The axisymmetric, funnel-shaped, computational domain shown in Fig. 3 is used for all simulations presented in this paper. As can be seen from this figure, the domain extends $30D_j$ radially and $50D_j$ axially away from the nozzle exit. The inlet to the nozzle is placed $1.5D_j$ upstream of the nozzle exit. At this boundary, non-uniform profiles of stagnation temperature and stagnation pressure are imposed. These profiles are selected to ensure that the mean velocity matches the experimental data as closely as possible at the nozzle exit. In addition to the mean velocity, several studies have demonstrated the importance of getting the turbulence levels at the nozzle exit right [37, 45, 67]. In order to accomplish this, the boundary layer must be sufficiently well resolved. In addition to this, injection of synthetic turbulence at the inlet and/or some tripping technique [37, 41, 67, 70] may be needed, especially if only a short part of the nozzle is included in the simulation. In this work, no synthetic turbulence or tripping technique is used. As will be explained in more detail later, the resolution close to the nozzle wall is also relatively low. This typically motivates the use of a wall-model or a hybrid RANS-LES model. Unfortunately, Nektar++ currently does not provide any wall models.

5

Therefore, a no-slip boundary condition is used for all walls instead. As a result of the wall modeling used in this work, the turbulence levels predicted by the simulations will not agree perfectly with the experimental data at the nozzle exit.

Along the far-field boundaries, a small co-flow corresponding to 2% of the jet velocity is added to the ambient state. This is done to ensure that vortical structures generated in the jet are removed from the domain as well as to facilitate flow entrainment. All boundary conditions are imposed weakly through the Riemann solver [52]. This implies that the far-field boundaries, where a complete thermodynamic state is imposed, will be non-reflecting for normally incident waves if the Riemann solver correctly differentiates between incoming and outgoing waves. The Riemann solver selected in this work approximately satisfies this condition.

Finally, at the outlet, the far-field static pressure is imposed. This boundary condition is perfectly reflective. Therefore, we add a sponge zone [71] upstream of the outlet, see Fig. 3. In this zone, the right-hand side of the governing equations is augmented with a damping term in order to drive the solution towards a steady reference state. The reference state is obtained with STAR-CCM+ v2019.2 using the $k - \omega$ SST turbulence model. More details on how the sponge zone is implemented are presented in [12].
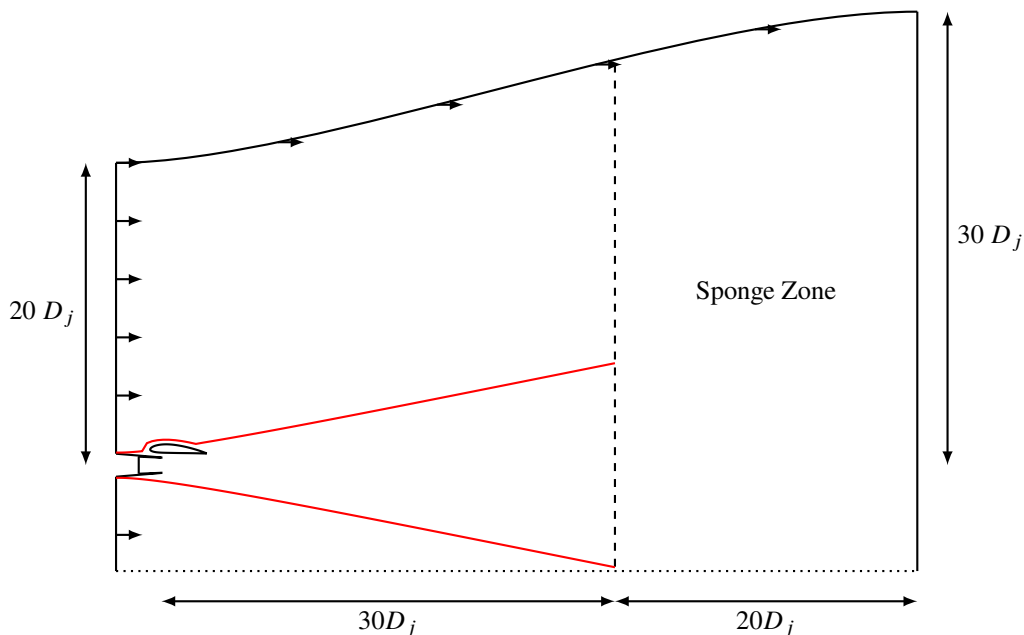

Fig. 3   Schematic view of the computational domain and the Ffowcs Williams - Hawkings integration surface.

2. Computational Mesh

The meshing procedure described in [13] was used to generate three meshes; one for the isolated round nozzle, one for the installed round nozzle, and one for the installed chevron nozzle. The first mesh, denoted "Mesh-1", is illustrated in Figs. 4a and 4b. As can be seen from these figures, the mesh is refined to resolve the shear layer and the jet plume up to the location of the Ffowcs Williams - Hawkings integration surface. The second mesh, denoted "Mesh-2", is illustrated in Figs. 4c and 4d. This mesh is almost identical to the first mesh, except that it includes the wing and that the resolution is slightly lower far downstream of the nozzle. The first two meshes were previously used in [13] to study the noise generated by the isolated and installed round nozzle. The third mesh, denoted "Mesh-3", is illustrated in Figs. 4e and 4f. This mesh has the same resolution as Mesh-2, except at the nozzle lip, where the mesh has been adapted for the chevrons. In particular, we mesh the chevron nozzle lip with isotropic mesh elements, whereas we use anisotropic mesh elements for the round nozzle lip. The reason we use anisotropic mesh elements for round nozzle is that this makes it possible to obtain a prism layer mesh where the elements in the last layer are close to isotropic. This will in turn create a good interface between the prism layer mesh and the surrounding tetrahedral mesh. Unfortunately, we were not able to create an anisotropic surface mesh for the chevron nozzle. To partly compensate for this, the thickness of the prism layer was reduced at the nozzle lip, as shown in Fig. 4f.
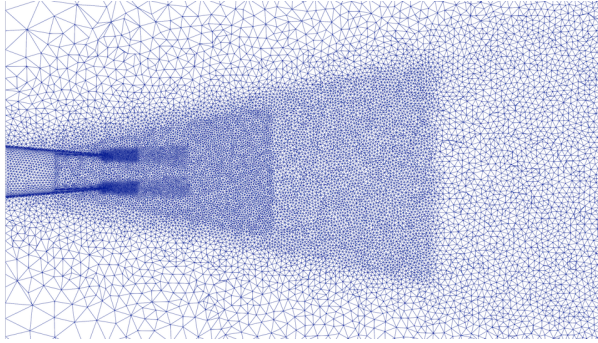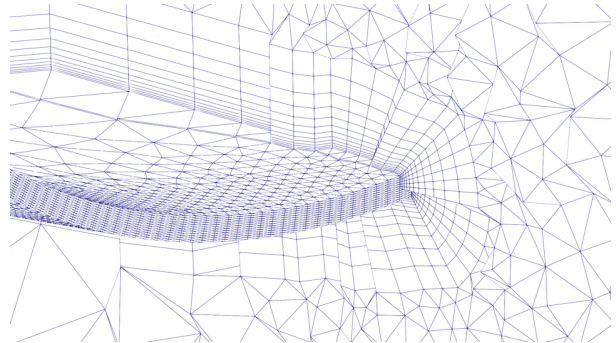
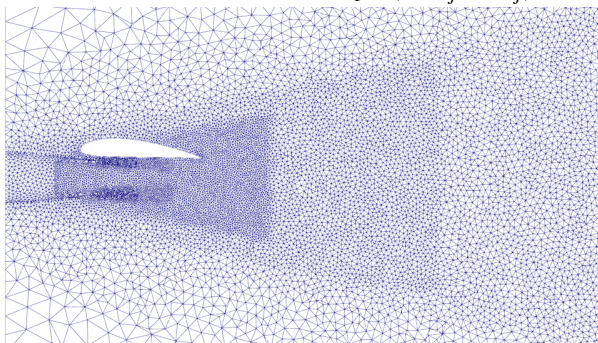(a) Overview of Mesh-1 for $x_1 \in (-3D_j, 15D_j)$.
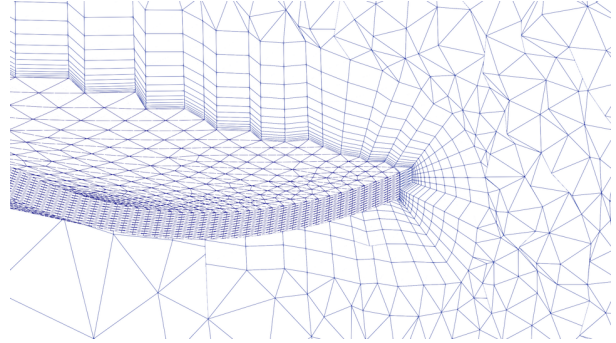
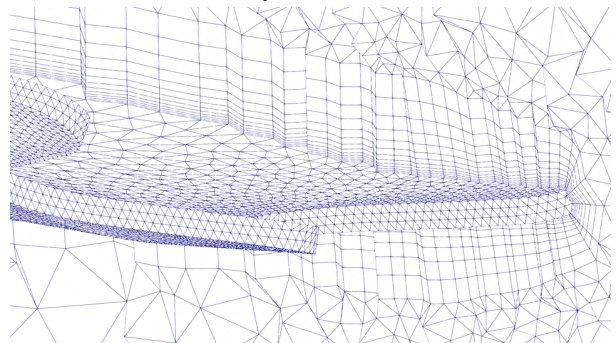(b) Prism layer mesh for Mesh-1.
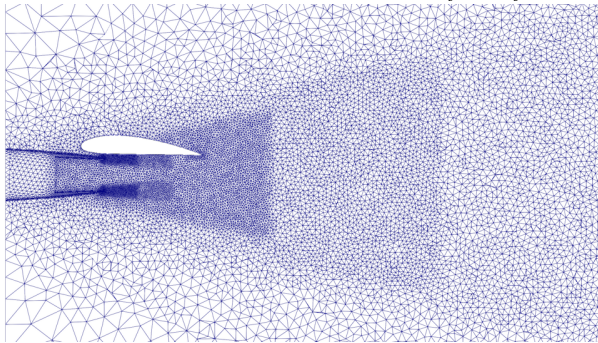
(c) Overview of Mesh-2 for $x_1 \in (-3D_j, 15D_j)$.

(d) Prism layer mesh for Mesh-2.

(e) Overview of Mesh-3 for $x_1 \in (-3D_j, 15D_j)$.

(f) Prism layer mesh for Mesh-3.

Fig. 4   Illustrations of the unstructured grids listed in Table 1.

In all three meshes, the boundary layer inside the nozzle is discretized with 13 elements in the wall normal direction, and one element per boundary layer thickness in the streamwise and spanwise directions. Here, the boundary layer thickness is estimated from the experimental data obtained at the nozzle exit for the isolated round nozzle, and is equal to $\delta_{99}/D_j = 0.048$. We emphasize that, for the polynomial degrees used in this work (see Table 2 for details), the chosen mesh resolution is not high enough to accurately resolve the turbulent boundary layer. In particular, even if a wall model was used, the resolution in the streamwise and spanwise directions would have had to be larger [72]. A summary of all meshes used in this work is provided in Table 1.

Table 1   Mesh settings.

Name	Configuration	N_{prism}	N_{tet}
Mesh-1	Isolated Round Nozzle	$4.36 \cdot 10^5$	$6.18 \cdot 10^6$
Mesh-2	Installed Round Nozzle	$4.63 \cdot 10^5$	$4.54 \cdot 10^6$
Mesh-3	Installed Chevron Nozzle	$9.26 \cdot 10^5$	$4.92 \cdot 10^6$

3. Simulation Parameters

Three simulations will be presented in this paper, one for each configuration. The simulation of the isolated nozzle was performed with a polynomial degree of $P = 2$, whereas the two simulations of the installed nozzles (with and without chevrons) were performed with $P = 3$. Previous work showed a significant improvement of the results for the installed round nozzle when going from $P = 2$ to $P = 3$ on the same mesh that we use in this work [13]. Therefore, it was decided to assess the influence of the chevrons using the higher polynomial degree ($P = 3$). Unfortunately, no simulation of the isolated nozzle with $P = 3$ was available at the time of writing this paper.

The simulation of the isolated nozzle was initialized with a steady RANS solution obtained with STAR-CCM+ v2019.2 using the $k - \omega$ SST turbulence model. After this, the simulation was run for 350 non-dimensional (acoustic) time units to bypass the initial transient. Finally, the simulation was run for another 320 non-dimensional time units. During this time, the conservative variables were sampled every 20th time step at a set of linear arrays in the jet plume. Since the flow is statistically axisymmetric for the isolated jet, 8 arrays were placed uniformly around the circumference such that statistical quantities could be averaged. In addition to sampling the flow field, data was also collected every 20th time step on the Ffowcs Williams - Hawkings integration surface. In this work, we use a conical surface that has a radius of $0.75D_j$ at the nozzle exit, a spreading rate of 0.2, and a total length of $30D_j$. Earlier work has shown that this surface is wide enough to enclose all relevant noise sources [12]. The time step used in the simulation of the isolated jet was set to $\Delta t^* = 0.002$.

The simulation of the installed round nozzle was started from a $P = 2$ solution on the same mesh. The $P = 2$ solution was in turn obtained by running the solver for 250 non-dimensional time units, starting from a steady RANS solution obtained using the same settings as for the isolated nozzle, see [13] for details. The $P = 3$ simulation of the installed round nozzle was first run for 300 non-dimensional time units to bypass the initial transient. After this, the simulation was sampled for 450 non-dimensional time units. During this time, the conservative variables were saved every 20th time step at a set of linear arrays in the jet plume. However, since the installed jet is not axisymmetric, additional arrays for averaging statistical quantities in the circumferential direction were not used. The flow was also stored every 20th time step at the Ffowcs Williams - Hawkings integration surface. This surface was constructed by combining the conical surface used for the isolated jet with a wing-shaped surface that encloses the wing. This relatively simple topology is believed to be sufficient since no flight stream is considered, which in turn means that the wing does not create a wake and/or wing-tip vortex. If the effect of a flight stream is considered, more sophisticated surfaces should be used [38]. The time step used for the installed round nozzle was also set to $\Delta t^* = 0.002$.

The simulation of the installed chevron nozzle was initialized from a steady RANS solution. After this, it was run for 350 non-dimensional time units before sampling was started. The flow was then sampled for 375 additional time units at the same rate as the installed round nozzle, both inside the jet and at the Ffowcs Williams - Hawkings integration surface. However, in contrast to the previous two simulations, the time step had to be lowered to $\Delta t^* = 0.001$ for the installed chevron nozzle. As a result, data were only collected at every 40th time step for the installed chevron nozzle.

A summary of the settings used for each simulation presented in this paper is provided in Table 2. The column denoted St_{lim} in this table provides an estimate of the highest Strouhal number that can be predicted by the simulation in the far-field. To obtain this estimate, the mesh resolution and polynomial degree at the Ffowcs Williams - Hawkings

integration surface were combined with the dissipation properties of the DG discretization according to the analysis presented in [13]. Details about the mesh resolution for Mesh-1 and Mesh-2 can also be found in [13] (note that the meshes are named differently in this paper). Since Mesh-3 is equivalent to Mesh-2 except very close to the nozzle lip, details about Mesh-3 can also be obtained from [13].

Table 2 **Simulation settings.** Δt_{jet} **and** $\Delta t_{\text{FW}-\text{H}}$ **denote the sampling time step (sampling rate) in the jet plume and on the Ffowcs Williams - Hawkings integration surface, respectively.** τ_{init} **and** τ_{sample} **denote the time the simulation is run before and during sampling, respectively.**

Name	P	Mesh	DOF	Initialize from	$\frac{\Delta t\, c_\infty}{D_j}$	$\frac{\Delta t_{\text{jet}}\, c_\infty}{D_j}$	$\frac{\Delta t_{\text{FW}-\text{H}}\, c_\infty}{D_j}$	$\frac{\tau_{\text{init}}\, c_\infty}{D_j}$	$\frac{\tau_{\text{sample}}\, c_\infty}{D_j}$	St_{lim}
Isolated-1	2	Mesh-1	$70 \cdot 10^6$	RANS	0.002	0.04	0.04	350	320	10.5
Installed-1	3	Mesh-2	$115 \cdot 10^6$	LES	0.002	0.04	0.04	300	450	11.1
Chevron-1	3	Mesh-3	$136 \cdot 10^6$	RANS	0.001	0.04	0.04	350	375	11.1

V. Experimental Setup

The experimental data used in this paper were recorded in the Doak Laboratory Flight Jet Rig (FJR), located at the University of Southampton. The following sub-sections present information about the facility, instrumentation, and experimental data post-processing.

A. Facility and Hardware

The Doak Laboratory is an anechoic chamber, fully anechoic above 400 Hz with dimensions approximately equal to 15 m-long, 7 m-wide and 5 m-high. The recently commissioned Flight Jet Rig (FJR) consists of two separate air supply systems that allow in-flight simulations of single-stream, subsonic jet flows. The primary 'core' jet flow is supplied by a high-pressure compressor-reservoir system, capable of producing a maximum inlet pressure of 20 Bar. The secondary 'flight' jet flow is supplied by a 1.1 pressure ratio fan. The 300 mm-diameter flight nozzle can produce flow velocities up to Mach 0.3. Photographs of the Doak Laboratory during the far-field, near-field, and flow-field campaigns are displayed in Fig. 5. Further information about the Doak Laboratory, the FJR, and the flight and core jet nozzles can be found in reference [51].

B. Instrumentation

A DANTEC StreamLine Pro constant temperature anemometry system was used to acquire the instantaneous velocity field and local flow temperature data. A DANTEC 55P11 miniature platinum-plated tungsten hot-wire probe, held by a DANTEC 55H22 right-angled probe support, was attached to an ISEL 3-axis traverse system, which allowed 600 mm-stroke (i.e., $15D_j$) independent movement along each of the x, y and z planes. Less exhaustive tests using DANTEC 55P61 cross-wires were also performed. A DANTEC 90P10 total temperature probe was secured near the sensors to account for local temperature variations in the flow. Hot-wire and cross-wire probes were calibrated at both the start and end of the test campaign using a DANTEC StreamLine automatic calibrator over the velocity range 1 - 300 m/s. The calibration coefficients were then extracted using a fourth-order polynomial curve fit. Finally, directional calibration was carried out for cross-wire probes to obtain information on the transverse velocity components.

To obtain far-field pressure data, ten 1/4" B&K Type 4939 microphone capsules with B&K Type 2670 Falcon preamplifiers were fixed to the end of 0.5m-long aluminium tubes and secured to a linear aluminium truss on the ceiling of the laboratory (i.e., at $\phi = 0°$) such that each microphone diaphragm was parallel to the jet axis. The microphones were positioned to record data at observer polar angles between $\theta = 40°$ and $\theta = 130°$, at $10°$ intervals. Each microphone was calibrated at both the start and end of the test campaign using a 94dB 1000kHz tone generated by a SVANTEK SV30A calibrator.

The near-field azimuthal microphone array consisted of eight 1/4" B&K Type 4939 microphone capsules with B&K Type 2670 Falcon preamplifiers fixed at the end of 0.5m-long aluminium tubes. The tubes were threaded through machined holes in aluminium blocks secured to a rigid aluminium alloy ring at $\Delta\phi = 45°$ intervals and then held in place with nylon grub screws such that each microphone pointed directly at the centre of the ring. The ring was then attached to an ISEL 2-axis traverse system and aligned with the jet axis using a nozzle laser jig.
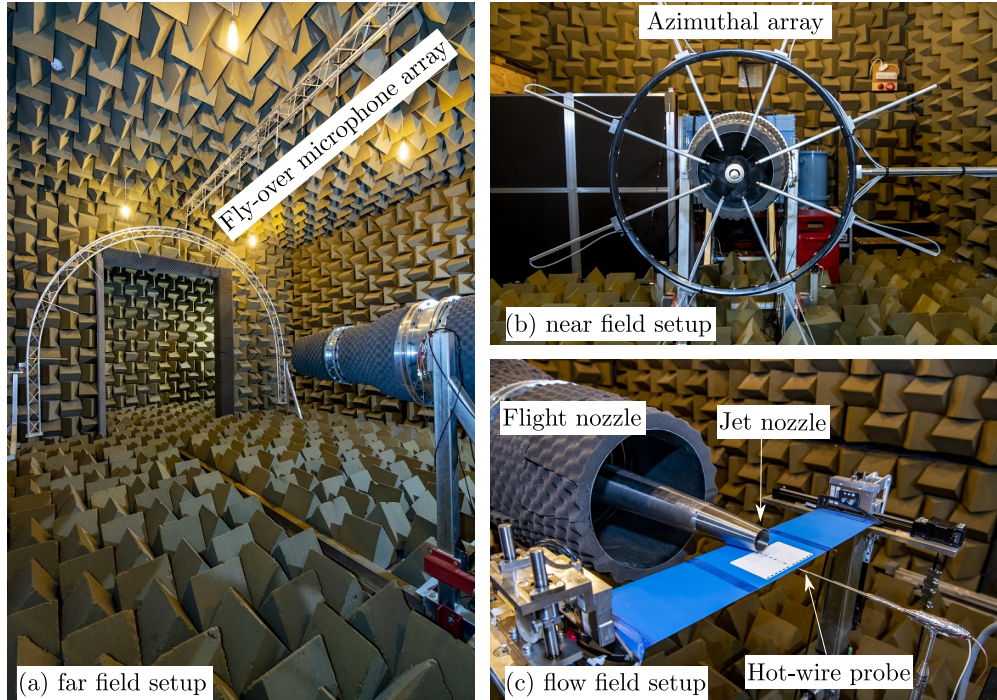
Fig. 5 Photographs of the Flight Jet Rig (FJR) in the Doak Laboratory at the University of Southampton.

C. Data Acquisition and Data Post-Processing

Both the hot-wire and microphone unsteady voltage data were digitised using a National Instruments PXIe-4497 Dynamic Signal Analyser at a sample rate of 200 kHz with 24-bit resolution. The hot-wire signals were acquired for 5 seconds, corrected first for temperature, using the standard method as reported by DANTEC [73], and then for velocity using the fourth-order polynomial calibration coefficients. Both the near-field and far-field microphone signals were acquired for 10 seconds, filtered using a 20 Hz high-pass filter and then amplified using B&K Type 2690 Nexus amplifiers. The time signals were corrected for amplifier gain and microphone capsule calibration sensitivity before they were transformed into the frequency domain using a Hamming window-averaged Fast Fourier Transform following Welch's overlapped segment-averaging spectral estimation method. The far-field spectra were then corrected for electronic background noise, atmospheric absorption, microphone incidence angle and distance (assuming spherical wave propagation) to yield the final free-field, 1m-lossless values. The near-field spectra were only corrected for electronic background noise.

Finally, the various rig flow control transducer data were digitised using the data acquisition hardware described above. Mean values were extracted from the voltage time histories before the appropriate calibration transfer function constants were applied. The total temperatures of the flight and core jet flows were recorded directly using two National Instruments USB-TC01 devices.

VI. Results

In this section, we present the results obtained from the simulations listed in Table 2. We will focus on the simulations of the two installed nozzles (with and without chevrons) and only include results for the isolated nozzle as a reference where needed. When results of the isolated nozzle are shown, it is important to keep in mind that this simulation was run with a lower polynomial degree, and thus a lower resolution, than the simulations of the installed nozzles. As a result, the difference between the isolated and installed simulations will not only be due to installation effects, but also due to differences in resolution.

A. Flow Statistics

Figures 6 and 7 show the mean axial velocity at several planes downstream of the nozzle exit for the two installed configurations listed in Table 2. As can be seen from these figures, the effect of the chevrons is clearly visible for $x_1/D_j \leq 2$. At $x_1/D_j = 3$, however, the mean velocity obtained with the chevron nozzle looks very similar to the one obtained with the round nozzle. Another interesting thing that can be noted from Fig. 7b is that the flow is slightly distorted close to the wing, likely as a result of the Coandă effect. This effect should also be present for the round nozzle, but since the flow field is almost axisymmetric, it is not as clearly visible.

The RMS of the axial velocity at several planes downstream of the nozzle exit is shown in Fig. 8 for the installed round nozzle and in Fig. 9 for the installed chevron nozzle. By comparing these figures, we can see that the peak turbulence levels in the early shear layer are relatively similar in the two simulations for $x_1/D_j \leq 1$. Further downstream, however, it is clear that the peak turbulence levels are lower for the chevron nozzle. In particular, at $x_1/D_j = 3$, where the trailing edge of the wing is located, the turbulence levels are significantly lower for the chevron nozzle. These observations are consistent with the ones reported by [74] for a closely installed chevron nozzle jet with the same number of serrations. This should translate into lower pressure fluctuations on the wing surface, which in turn might contribute to lower noise levels in the far-field.

(a) $x_1/D_j = 0.25$.

(b) $x_1/D_j = 0.5$.

(c) $x_1/D_j = 1$.

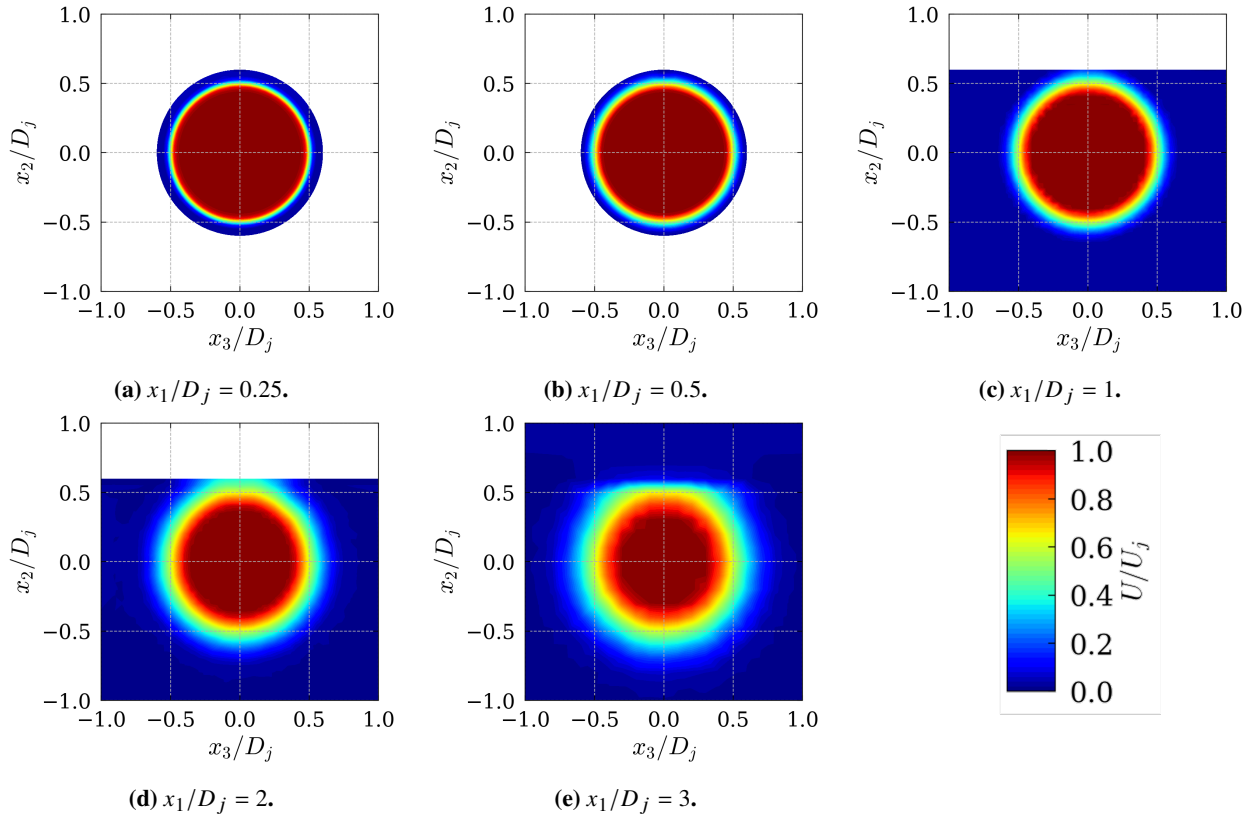(d) $x_1/D_j = 2$.

(e) $x_1/D_j = 3$.

Fig. 6 Mean axial velocity at several planes downstream of the nozzle exit obtained with the simulation denoted Installed-1 in Table 2. For the first two planes, only a limited radial extent of the flow was sampled.
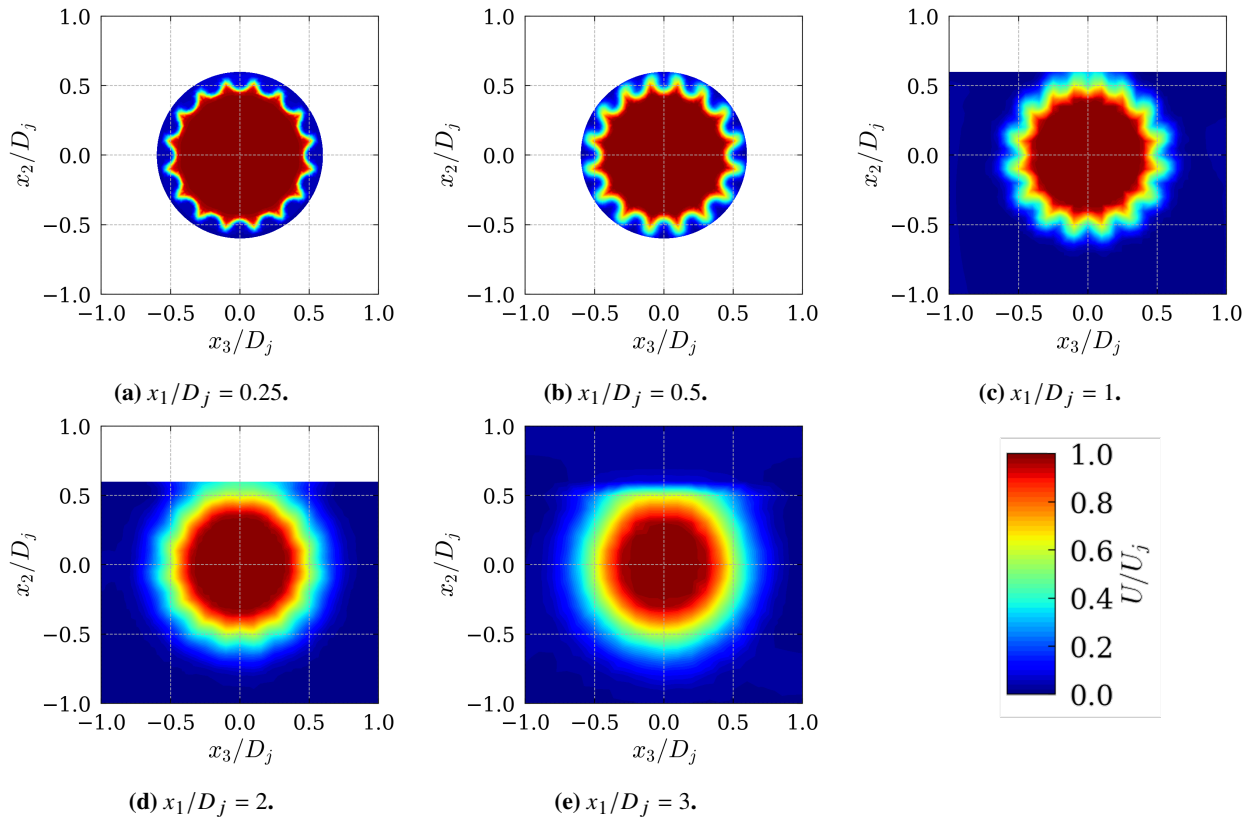
11

(a) $x_1/D_j = 0.25$.

(b) $x_1/D_j = 0.5$.

(c) $x_1/D_j = 1$.

(d) $x_1/D_j = 2$.

(e) $x_1/D_j = 3$.

Fig. 7 **Mean axial velocity at several planes downstream of the nozzle exit obtained with the simulation denoted Chevron-1 in Table 2. For the first two planes, only a limited radial extent of the flow was sampled.**

12

(a) $x_1/D_j = 0.25$.

(b) $x_1/D_j = 0.5$.

(c) $x_1/D_j = 1$.

(d) $x_1/D_j = 2$.
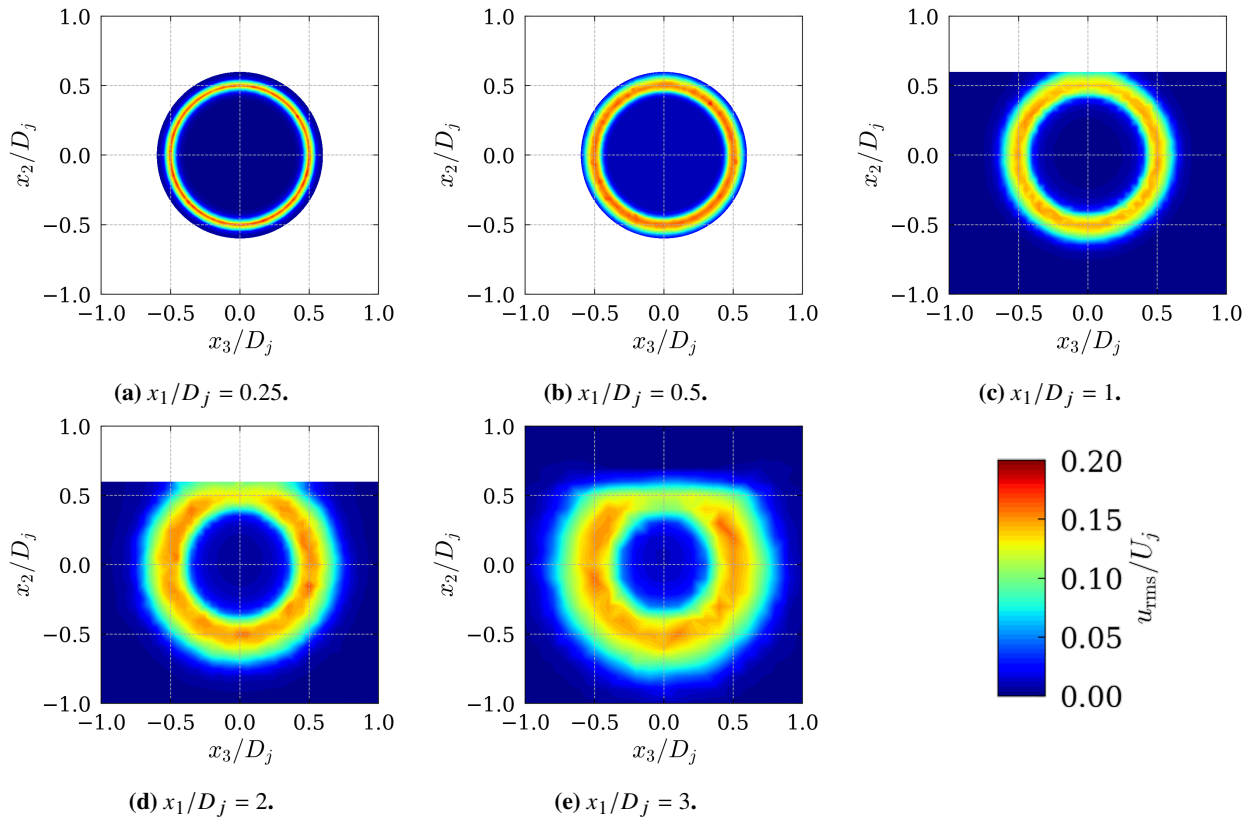
(e) $x_1/D_j = 3$.

Fig. 8   RMS of the axial velocity at several planes downstream of the nozzle exit obtained with the simulation denoted Installed-1 in Table 2. For the first two planes, only a limited radial extent of the flow was sampled.
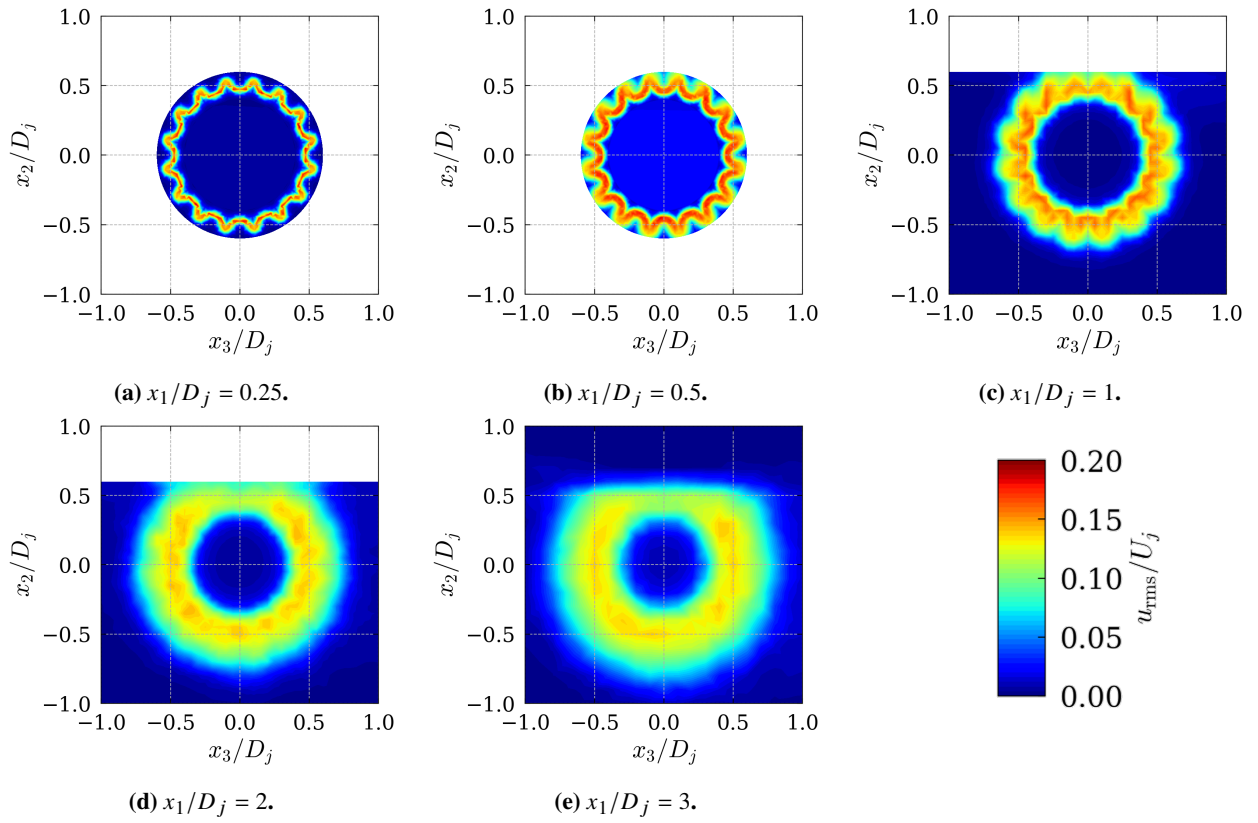
13

(a) $x_1/D_j = 0.25$.

(b) $x_1/D_j = 0.5$.

(c) $x_1/D_j = 1$.

(d) $x_1/D_j = 2$.

(e) $x_1/D_j = 3$.

Fig. 9 **RMS of the axial velocity at several planes downstream of the nozzle exit obtained with the simulation denoted Chevron-1 in Table 2. For the first two planes, only a limited radial extent of the flow was sampled.**

The mean axial velocity at the nozzle exit ($x_1/D_j = 0.005$) is shown in Fig. 10a. In this figure, we have included results from all simulations listed in Table 2, as well as experimental results for the isolated round nozzle. No experimental data for the installed nozzle, with or without chevrons, are currently available for reference. As can be seen from Fig. 10a, the two simulations of the round nozzle agree relatively well with each other, and with the experimental data. This is expected, since we imposed tailored profiles of the stagnation temperature and stagnation pressure at the inlet to the nozzle. The results for the chevron nozzle, on the other hand, deviate slightly from the other results. This is likely due to the fact that the chevrons effectively extend the length of the nozzle, which in turn means that the flow has not reached its peak velocity at $x_1/D_j = 0.005$, where the data shown in Fig. 10a were collected. Indeed, as will be shown later when looking at the mean velocity along the centerline, the simulation of the chevron nozzle reaches the same peak velocity as the simulations of the round nozzles slightly further downstream.

Next, we turn to Fig. 10b, which shows the RMS of the axial velocity at the nozzle exit. As can be seen from this figure, the simulation of the isolated round nozzle under-predicts the turbulence levels at the nozzle exit. The two simulations of the installed nozzle, on the other hand, over-predict the turbulence levels in the boundary layer. The higher turbulence levels obtained for the two simulations of the round nozzle are most likely related to the higher polynomial degree used in these simulations. As explained earlier, none of the simulations performed in this work resolve the boundary layer with sufficient accuracy. Therefore, we can not expect the turbulence levels in the boundary layer to be correct. Fig. 10b reflects this fact, and highlights the need for better modeling of the boundary layer in future work. This is especially important for jet aeroacoustics, as shown by several recent studies [37, 45, 67].
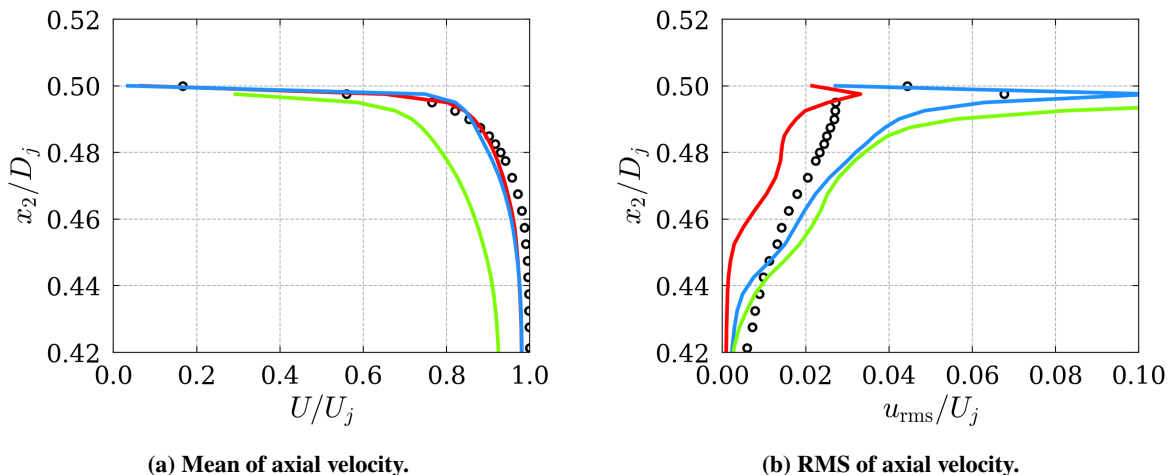

(a) Mean of axial velocity.

(b) RMS of axial velocity.

Fig. 10 **Axial velocity statistics at the nozzle exit: Isolated-1 (——), Installed-1 (——), Chevron-1 (——), Experiments for isolated round nozzle (○).**

The mean of the axial velocity at several locations in the jet plume obtained for the two installed configurations is shown in Fig. 11a. As can be seen from this figure, the two simulations of the installed nozzle give virtually identical results, except close to the nozzle exit, where the velocity profile predicted by the chevron nozzle is slightly narrower. This narrower velocity profile is a direct result of the way the chevrons are located around the circumference. In particular, one chevron is positioned at the top, and one at the bottom, leading to a contraction of the flow in the $x_3 = 0$ plane. This is also clearly visible from Fig. 7. In addition to this, the Coandă effect mentioned earlier is visible in the mean velocity profiles.

The RMS of the axial velocity at several locations in the jet plume is shown in Fig. 11b. Apart from small differences in the peak turbulence levels (especially around $x_1/D_j = 3$), and a small differences in shape due to the contraction of the jet in the $x_3 = 0$ plane, the turbulence levels predicted by the round and chevron nozzle are very similar. It is also worth noting that the turbulence levels are lower close to the wing compared to the other side of the jet axis.

The experimental data shown in Fig. 11 were obtained for the installed round nozzle. Unfortunately, no data was available for the chevron nozzle at the time of writing this paper. Therefore, we can only comment on the accuracy of the simulation of the installed round nozzle. For this simulation, we see quite favourable agreement with the experiments, both for the mean and the RMS of the axial velocity. The most notable differences are observed close to the centerline, where the turbulence levels are under-predicted by the simulation. In addition to this, we can see that the peak velocity

15

close to the centerline is over-predicted by the simulations for $x_1/D_j > 6$. These discrepancies may be a result of insufficient turbulent mixing in the shear layer, which in turn could be related to the state of the boundary layer at the nozzle exit and/or the resolution in the jet plume. Another possible cause of the discrepancies is the mean velocity at the nozzle exit. In reality, the flow should contain a small radial velocity component at the nozzle exit due to the nozzle contraction. In the simulations, however, an axial flow is imposed shortly upstream of the nozzle exit. As a result, the mean radial velocity will likely not perfectly match the experiment.
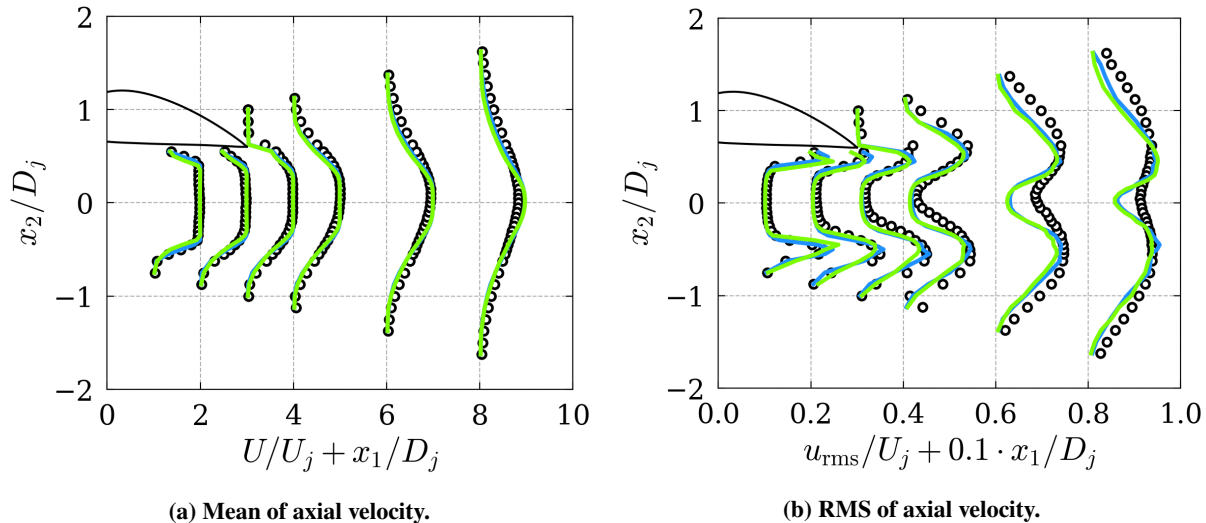

| (a) Mean of axial velocity. | (b) RMS of axial velocity. |

Fig. 11 **Axial velocity statistics in the jet plume: Installed-1 (——), Chevron-1 (——), Experiments for installed round nozzle (○).**

The mean and the RMS of the axial velocity along the centerline obtained with all simulations listed in Table 2 are shown in Fig. 12. As can be seen from this figure, the results obtained with the installed round and the installed chevron nozzle are virtually identical. In particular, the length of the potential core is the same in both simulations. This is somewhat unexpected since chevrons typically increase mixing in the shear layer. Unfortunately, only experimental results for the isolated round nozzle were available at the time of writing this paper. Therefore, we can not say whether the similarity observed between the two installed nozzles shown in Fig. 12 are physically correct or not. It is, however, notable that all simulations predict a longer potential core and lower turbulence levels along the centerline than the experimental data for the isolated round nozzle. This is, once again, an indication that the flow conditions at the nozzle exit are not perfectly captured in the simulations. With regards to the difference observed between the isolated and installed results, one should keep in mind that different polynomial degrees were used in the two simulations.

The mean of the axial velocity along the lipline is shown in Fig. 13a. As can be seen from this figure, there is a notable difference between the isolated and installed round nozzle, and between the installed round and the installed chevron nozzle. In comparison to the isolated round nozzle, a small acceleration of the flow is visible around $x_1/D_j = 3$ for the installed round nozzle. This is expected for the closely installed configuration considered in this work. Further downstream, the results obtained for the isolated round nozzle also differ from the installed round nozzle. In this region, however, the discrepancies are believed to be related to the lower resolution used in the simulation of the isolated nozzle. When comparing the results obtained for the installed nozzle, with and without chevrons, it is clear that the mean velocity is lower for the chevron nozzle. As discussed previously, this is because the chevrons are positioned such that they direct the flow inwards at $(x_2/D_j, x_3/D_j) = (0.5, 0)$, see Fig. 7.

The redirection of the flow by the chevrons is also visible when looking at the RMS of the axial velocity along the lipline, shown in Fig. 13b. In particular, close to the nozzle, the lower levels obtained with the chevrons are mostly due to the fact that the shear layer is redirected inwards, resulting in lower turbulence levels at $x_2/D_j = 0.5$. However, as pointed out when the contours of the RMS of the axial velocity shown in Figs. 8 and 9 were discussed, the non-uniformity of the flow introduced by the chevrons has virtually disappeared at $x_1/D_j = 3$. In addition to this, the peak turbulence levels are lower at this point for the chevron nozzle. The last observation is also clearly visible in Fig. 13b. Finally, we note that the plots of the RMS of the axial velocity show clear peaks close to the nozzle lip, especially for the round nozzles where the measurement probes are located inside the shear layer. These peaks are likely associated with laminar

to turbulent transition, and are known to occur when the turbulence levels in the boundary layer are too low [45]. As can be seen from Fig. 13b, these peaks are not present in the experimental results for the isolated round nozzle (data for the installed nozzle, with or without chevrons, are not available at the time of writing this paper). This is another indication that the state of the boundary layer at the nozzle exit is not correctly captured in the simulations.
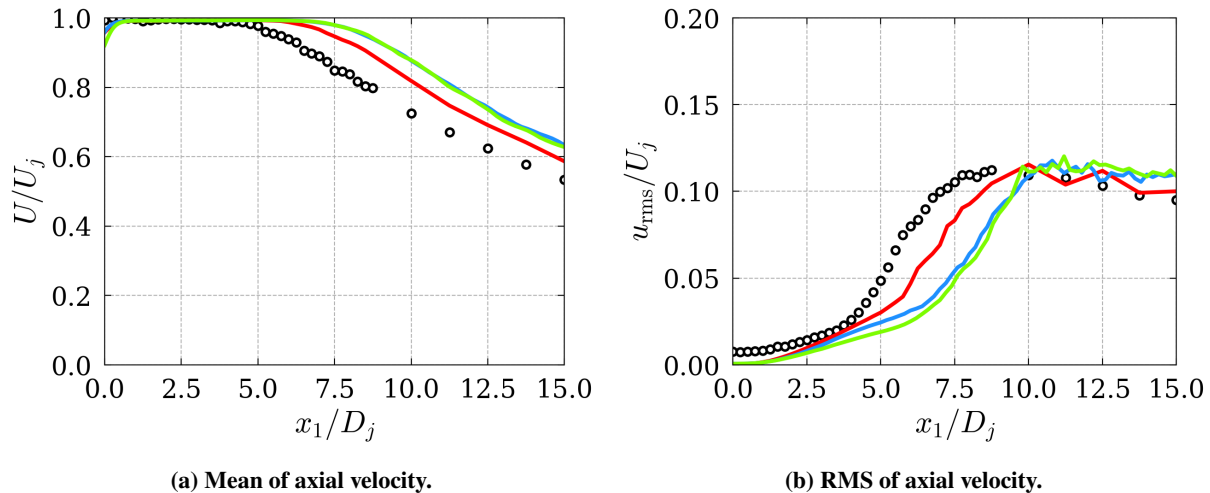

(a) Mean of axial velocity.

(b) RMS of axial velocity.

Fig. 12   Axial velocity statistics along centerline: Isolated-1 (——), Installed-1 (——), Chevron-1 (——), Experiments for isolated round nozzle (○).
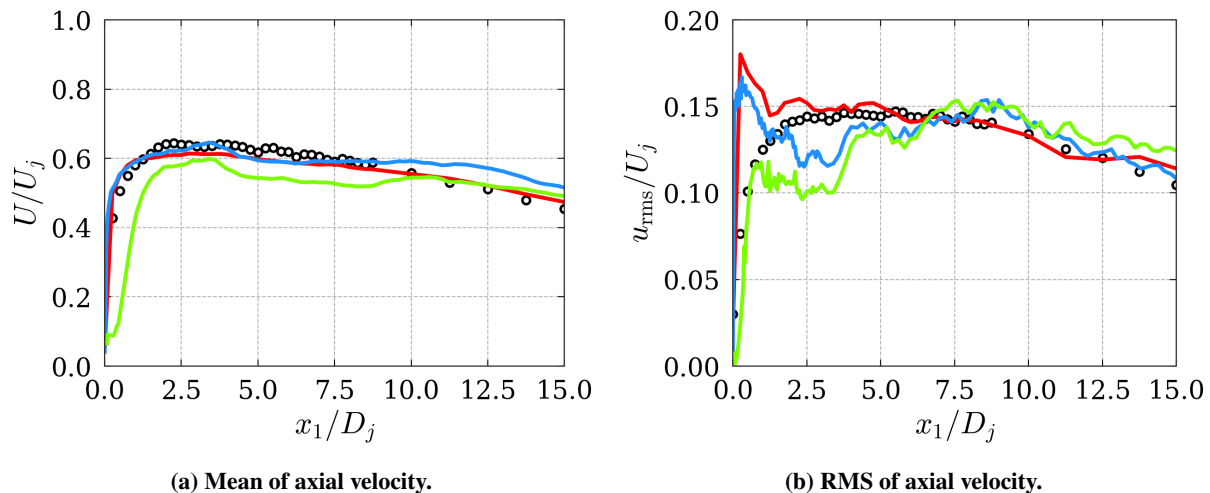

(a) Mean of axial velocity.

(b) RMS of axial velocity.

Fig. 13   Axial velocity statistics along lipline: Isolated-1 (——), Installed-1 (——), Chevron-1 (——), Experiments for isolated round nozzle (○).

B. Far-Field Acoustics

The OASPL computed from Eq. (3) is shown in Fig. 14. As can be seen from this figure, the installed round nozzle gives significantly higher noise levels for all observer positions than the isolated round nozzle. This is expected since installed nozzles generate additional noise due to scattering of the hydrodynamic pressure field at the airfoil trailing edge. In addition to this, noise generated close to the nozzle is reflected against the wing, and thus contribute to higher noise levels on the unshielded side of the wing, which is where the microphones are located. From Fig. 14, we can also see that the simulations predict a 1dB noise reduction across all observer angles for the chevron nozzle. This should be compared to the experiments, which show a 1.5dB noise reduction for the chevron nozzle. Lastly, we note that the

simulations of the installed nozzles agree significantly better with the experimental data than the simulation of the isolated nozzle. The larger discrepancy observed for the isolated nozzle is partly attributed to the lower resolution used for this nozzle. Indeed, previous work on the installed round nozzle showed that the far-field acoustic results improved when the polynomial degree was increased [13].
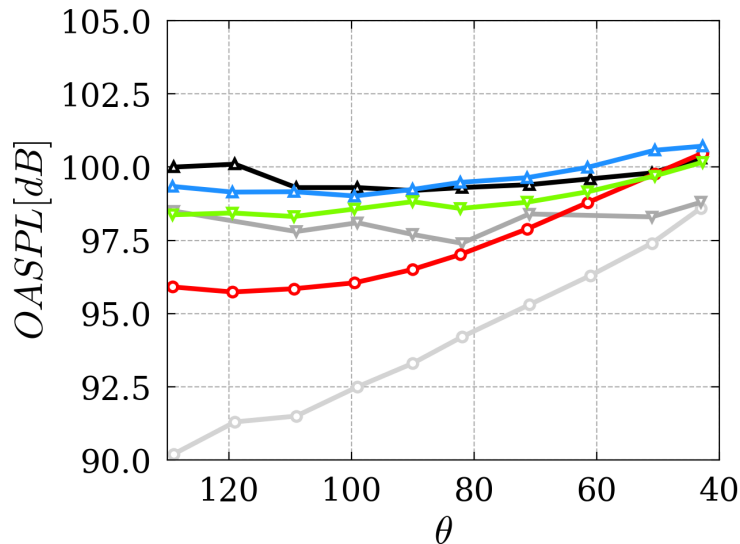

Fig. 14   Overall Sound Pressure Level (OASPL) obtained at the microphone locations shown in Fig. 2, and then normalized to 1m distance according to Eq. (3)**: Isolated-1 (——), Installed-1 (——), Chevron-1 (——), Experiments for isolated round nozzle (——), Experiments for installed round nozzle (——), Experiments for installed chevron nozzle (——).**

Next, we will consider the PSD of the pressure signal in the far-field. As explained in section IV.B, the PSD is computed using Welch's method. The number of time samples included in each segment in Welch's method is set to $N_{\text{FFT}} = 833$, leading to a frequency resolution of $\Delta St = D_j/(N_{\text{FFT}}\Delta t_{\text{FW}-\text{H}}U_j) = 0.05$. The Nyquist Strouhal number is further equal to $St_{\text{Nyq}} = D_j/(2\Delta t_{\text{FW}-\text{H}}U_j) = 20.83$. This number is approximately twice as large as the highest resolved Strouhal number estimated for the simulations, see Table 2 for details. For the isolated nozzle, the PSD is averaged over 36 microphones that are uniformly distributed around the circumference. For the installed nozzle, on the other hand, the PSD is only computed at the microphone locations shown in Fig. 2.

The PSDs obtained at four representative microphone locations are shown in Fig. 15. As can be seen from this figure, the two simulations of the installed nozzle give very similar results, both in terms of absolute levels and the shape of the spectra. There are, however, some notable differences in the frequency range $0.05 < St < 2$, where the simulation of the chevron nozzle gives lower noise levels. In this frequency range, we can also note that the simulations agree reasonable well with the corresponding experimental data. For lower and higher frequencies, the simulations under- and over-predict the experimental results, respectively. This issue has previously been discussed in [13]. Finally, we note that the experimental results for the two installed nozzles, with and without chevrons, look very similar. This small difference is consistent with the small difference observed in the simulation results, and with the fact that we observed relatively small differences in the aerodynamic results.
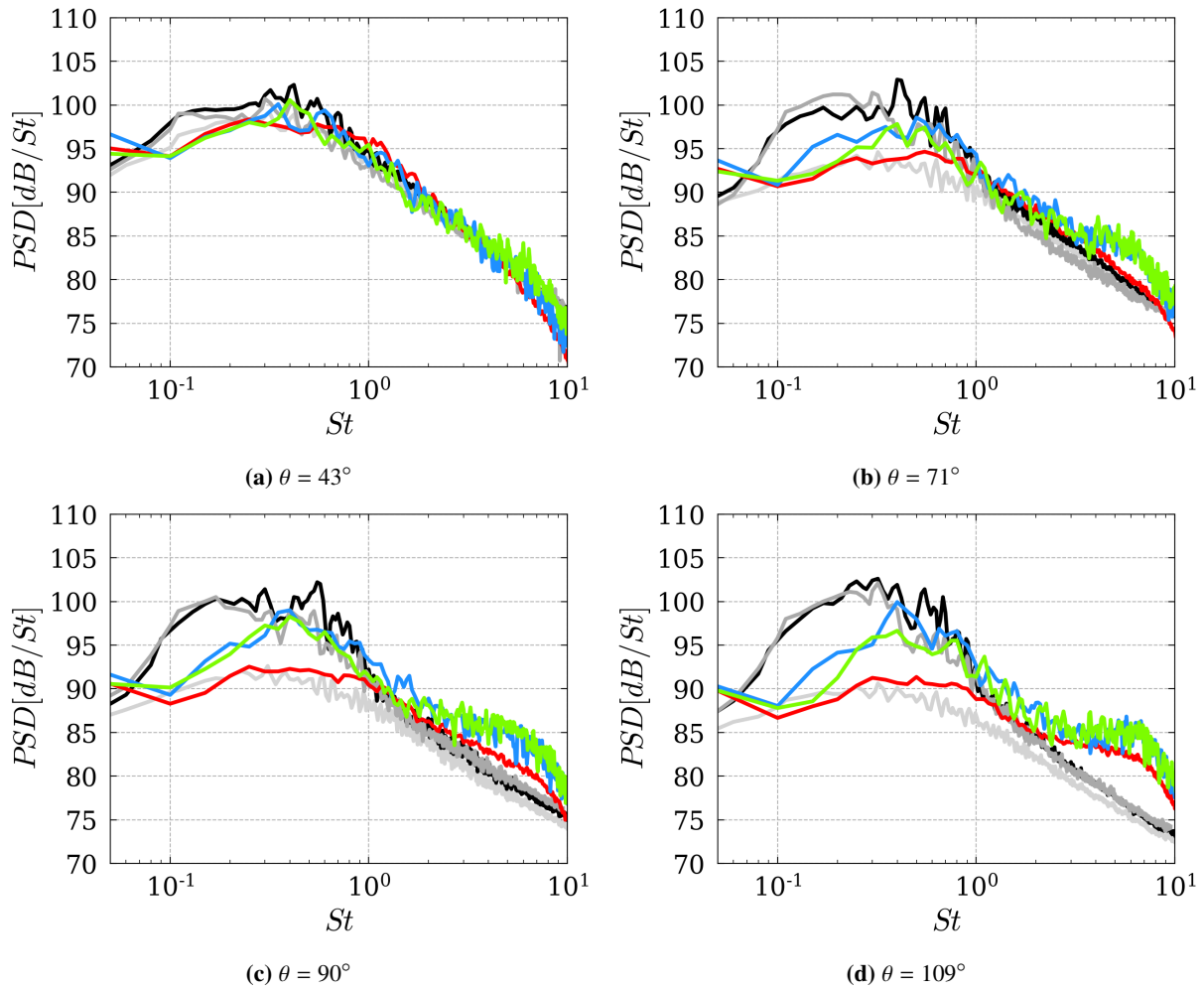
(a) $\theta = 43°$

(b) $\theta = 71°$

(c) $\theta = 90°$

(d) $\theta = 109°$

Fig. 15   Power spectral density in the far-field: Isolated-1 (──), Installed-1 (──), Chevron-1 (──) Experiments for isolated round nozzle (──), Experiments for installed round nozzle (──), Experiments for installed chevron nozzle (──).

VII. Conclusions

In this work we have used Large Eddy Simulations (LES) to study the influence of chevrons on the flow and noise fields produced by a closely installed jet. To this end, a baseline round nozzle is compared to a serrated nozzle with 16 chevrons. In both cases, the nozzle is installed under a NACA4415 airfoil such that the axial and vertical distance between the center of the nozzle exit and the airfoil trailing edge are $H/D_j = 0.6$ and $L/D_j = 3$, respectively. The nozzle operates at an acoustic Mach number of $M_a = 0.6$, a Reynolds number of $Re = 5.5 \cdot 10^5$, and a static temperature ratio of $T_j/T_\infty = 0.9335$.

In previous work [12, 13], experimental data from the Doak Laboratory Flight Jet Rig [51] were used to assess the accuracy of the simulation results for the isolated and installed round nozzle. In general, it was found that the aerodynamic results agreed reasonably well with the experiments, whereas some discrepancies were observed in the far-field acoustic results. These discrepancies were likely caused by insufficient modeling of the boundary layer inside the nozzle [12, 13]. Unfortunately, better modeling of the boundary layer using, e.g., a higher streamwise and spanwise resolution, a wall model, and/or artificial tripping of the boundary layer, were outside the scope of this work. However, even with state-of-the-art modeling of the boundary layer, Gand et al. [41] reported notable discrepancies in terms of the far-field noise levels for a similar $M = 0.6$ jet. Similarly, Shur et al. [75] reported notable discrepancies in the far-field noise predictions of a $M = 0.36$ jet compared to a $M = 0.9$ jet. These results indicate that it is harder to predict the noise produced by jets with lower Mach numbers. However, given that the trend in aviation is to move towards higher bypass ratio turbofan engines with a lower jet velocity, the need to accurately predict lower Mach number jets has probably never been greater.

Despite the aforementioned limitations, the simulations were able to capture the effect of the chevron nozzle to a good degree of accuracy. In particular, a noise reduction in the far-field of 1dB when compared to the installed round nozzle was obtained. This should be compared to the experiments, which predict a 1.5dB noise reduction for the installed chevron nozzle. In addition to this, the simulations provide a valuable insight into the aerodynamic field introduced by the chevrons.

References

[1] Lighthill, M. J., "Report on the Final Panel Discussion on Computational Aeroacoustics," ICASE Report No. 92-53, NASA, Hampton, VA, October 1992.

[2] Lighthill, M. J., "On Sound Generated Aerodynamically. I. General Theory," *Proceedings of the Royal Society of London. Series A, Mathematical and Physical Sciences*, Vol. 211, No. 1107, 1952, pp. 564–587. https://doi.org/10.1098/rspa.1952.0060.

[3] Lighthill, M. J., "On Sound Generated Aerodynamically. II. Turbulence as a Source of Sound," *Proceedings of the Royal Society of London. Series A, Mathematical and Physical Sciences*, Vol. 222, No. 1148, 1954, pp. 1–32. https://doi.org/10.1098/rspa.1954.0049.

[4] Lyu, B., Dowling, A. P., and Naqvi, I., "Prediction of installed jet noise," *Journal of Fluid Mechanics*, Vol. 811, 2017, p. 234–268. https://doi.org/10.1017/jfm.2016.747.

[5] Head, R., and Fisher, M., "Jet/surface interaction noise - Analysis of farfield low frequency augmentations of jet noise due to the presence of a solid shield," *3rd Aeroacoustics Conference*, Palo Alto, CA, 1976. https://doi.org/10.2514/6.1976-502.

[6] Mead, C., and Strange, P., "Under-wing installation effects on jet noise at sideline," *4th AIAA/CEAS Aeroacoustics Conference*, Toulouse, France, 1998. https://doi.org/10.2514/6.1998-2207.

[7] Rego, L., Avallone, F., Ragni, D., and Casalino, D., "On the mechanisms of jet-installation noise reduction with flow-permeable trailing edges," *Journal of Sound and Vibration*, Vol. 520, 2022. https://doi.org/10.1016/j.jsv.2021.116582.

[8] Jente, C., Schmidt, J., Delfs, J., Rossignol, K.-S., Pott-Pollenske, M., and Siller, H. A., "Noise reduction potential of flow permeable materials for jet-flap interaction noise," *28th AIAA/CEAS Aeroacoustics Conference*, Southampton, UK, 2022. https://doi.org/10.2514/6.2022-3040.

[9] Piantanida, S., Jaunet, V., Huber, J., Wolf, W. R., Jordan, P., and Cavalieri, A. V. G., "Scattering of turbulent-jet wavepackets by a swept trailing edge," *The Journal of the Acoustical Society of America*, Vol. 140, No. 6, 2016, pp. 4350–4359. https://doi.org/10.1121/1.4971425.

[10] Ugur Karban, P. J., Eduardo Martini, "Modeling closed-loop control of installation noise using Ginzburg-Landau equation," , 2023. https://doi.org/10.48550/arXiv.2303.03176.

[11] Zaman, K., Bridges, J., and Huff, D., "Evolution from 'Tabs' to 'Chevron Technology' - A Review," *International Journal of Aeroacoustics*, Vol. 10, No. 5-6, 2011, pp. 685–709. https://doi.org/10.1260/1475-472X.10.5-6.685.

[12] Lindblad, D., Sherwin, S., Cantwell, C., Lawrence, J., Proenca, A., and Moragues Ginard, M., "Aeroacoustic Analysis of a Subsonic Jet using the Discontinuous Galerkin Method," *28th AIAA/CEAS Aeroacoustics Conference*, Southampton, UK, 2022. https://doi.org/10.2514/6.2022-2932.

[13] Lindblad, D., Sherwin, S. J., Cantwell, C. D., Lawrence, J. L. T., Proenca, A. R., and Moragues Ginard, M., "Large Eddy Simulations of Isolated and Installed Jet Noise using the High-Order Discontinuous Galerkin Method," *AIAA SciTech 2023 Forum*, National Harbor, MD, 2023. https://doi.org/10.2514/6.2023-1546.

[14] Cantwell, C., Moxey, D., Comerford, A., Bolis, A., Rocco, G., Mengaldo, G., De Grazia, D., Yakovlev, S., Lombard, J.-E., Ekelschot, D., Jordi, B., Xu, H., Mohamied, Y., Eskilsson, C., Nelson, B., Vos, P., Biotto, C., Kirby, R., and Sherwin, S., "Nektar++: An open-source spectral/hp element framework," *Computer Physics Communications*, Vol. 192, 2015, pp. 205 – 219. https://doi.org/10.1016/j.cpc.2015.02.008.

[15] Moxey, D., Cantwell, C. D., Bao, Y., Cassinelli, A., Castiglioni, G., Chun, S., Juda, E., Kazemi, E., Lackhove, K., Marcon, J., Mengaldo, G., Serson, D., Turner, M., Xu, H., Peiró, J., Kirby, R. M., and Sherwin, S. J., "Nektar++: Enhancing the capability and application of high-fidelity spectral/hp element methods," *Computer Physics Communications*, Vol. 249, 2020. https://doi.org/10.1016/j.cpc.2019.107110.

[16] antares Development Team, "Antares Documentation Release 1.17.0," , 2020. URL https://cerfacs.fr/antares/.

[17] Di Stefano, D., Rona, A., Hall, E., and Puigt, G., "Implementing the Ffowcs Williams and Hawkings acoustic analogy in Antares," *The 22nd International Congress on Sound and Vibration (ICSV22)*, Florence, Italy, 2015.

[18] Di Stefano, D., Rona, A., Hall, E., Morfey, C. L., and Puigt, G., "Validating the Ffowcs Williams and Hawkings acoustic analogy implementation in Antares," *22nd AIAA/CEAS Aeroacoustics Conference*, Lyon, France, 2016. https://doi.org/10.2514/6.2016-3059.

[19] Reed, W. H., and Hill, T., "Triangular mesh methods for the neutron transport equation," Technical Report LA-UR-73-479, Los Alamos Scientific Laboratory, 1973.

[20] Cockburn, B., Karniadakis, G. E., and Shu, C.-W., "The Development of Discontinuous Galerkin Methods," *Discontinuous Galerkin Methods*, Springer Berlin Heidelberg, Berlin, Heidelberg, 2000, pp. 3–50. https://doi.org/10.1007/978-3-642-59721-3_1.

[21] Mengaldo, G., "Discontinuous spectral/hp element methods: development, analysis and applications to compressible flows," Ph.D. thesis, Imperial College London, London, UK, 2015. https://doi.org/10.25560/28678.

[22] Yan, Z.-G., Pan, Y., Castiglioni, G., Hillewaert, K., Peiró, J., Moxey, D., and Sherwin, S. J., "Nektar++: Design and implementation of an implicit, spectral/hp element, compressible flow solver using a Jacobian-free Newton Krylov approach," *Computers & Mathematics with Applications*, Vol. 81, 2021, pp. 351–372. https://doi.org/10.1016/j.camwa.2020.03.009.

[23] Ffowcs Williams, J. E., and Hawkings, D. L., "Sound Generation by Turbulence and Surfaces in Arbitrary Motion," *Philosophical Transactions of the Royal Society of London. Series A, Mathematics and Physical Sciences*, Vol. 264, No. 1151, 1969, pp. 321–342. https://doi.org/10.1098/rsta.1969.0031.

[24] di Francescantonio, P., "A New Boundary Integral Formulation for the Prediction of Sound Radiation," *Journal of Sound and Vibration*, Vol. 202, No. 4, 1997, pp. 491–509. https://doi.org/10.1006/jsvi.1996.0843.

[25] Huynh, H. T., "A Flux Reconstruction Approach to High-Order Schemes Including Discontinuous Galerkin Methods," *18th AIAA Computational Fluid Dynamics Conference*, Miami, FL, 2007. https://doi.org/10.2514/6.2007-4079.

[26] Lorteau, M., de la Llave Plata, M., and Couaillier, V., "Turbulent jet simulation using high-order DG methods for aeroacoustic analysis," *International Journal of Heat and Fluid Flow*, Vol. 70, 2018, pp. 380 – 390. https://doi.org/10.1016/j.ijheatfluidflow.2018.01.012.

[27] Alhawwary, M. A., and Wang, Z. J., "Implementation of a FWH approach in a high-order LES tool for aeroacoustic noise predictions," *AIAA Scitech 2020 Forum*, Orlando, FL, 2020. https://doi.org/10.2514/6.2020-1724.

[28] Shur, M. L., Spalart, P. R., and Strelets, M. K., "Noise Prediction for Increasingly Complex Jets. Part I: Methods and Tests," *International Journal of Aeroacoustics*, Vol. 4, No. 3, 2005, pp. 213–245. https://doi.org/10.1260/1475472054771376.

[29] Andersson, N., Eriksson, L.-E., and Davidson, L., "Large-Eddy Simulation of Subsonic Turbulent Jets and Their Radiated Sound," *AIAA Journal*, Vol. 43, No. 9, 2005, pp. 1899–1912. https://doi.org/10.2514/1.13278.

[30] Shur, M. L., Spalart, P. R., and Strelets, M. K., "LES-based evaluation of a microjet noise reduction concept in static and flight conditions," *Journal of Sound and Vibration*, Vol. 330, No. 17, 2011, pp. 4083–4097. https://doi.org/10.1016/j.jsv.2011.02.013.

[31] Brès, G., Nichols, J., Lele, S., and Ham, F., "Towards Best Practices for Jet Noise Predictions with Unstructured Large Eddy Simulations," *42nd AIAA Fluid Dynamics Conference and Exhibit*, New Orleans, LA, 2012. https://doi.org/10.2514/6.2012-2965.

[32] Xia, H., and Tucker, P. G., "Numerical Simulation of Single-Stream Jets from a Serrated Nozzle," *Flow, Turbulence and Combustion*, Vol. 88, 2012, pp. 3–18. https://doi.org/10.1007/s10494-011-9377-5.

[33] Mendez, S., Shoeybi, M., Sharma, A., Ham, F. E., Lele, S. K., and Moin, P., "Large-Eddy Simulations of Perfectly Expanded Supersonic Jets Using an Unstructured Solver," *AIAA Journal*, Vol. 50, No. 5, 2012, pp. 1103–1118. https://doi.org/10.2514/1.J051211.

[34] Shur, M. L., Spalart, P. R., and Strelets, M. K., "Jet noise computation based on enhanced DES formulations accelerating the RANS-to-LES transition in free shear layers," *International Journal of Aeroacoustics*, Vol. 15, No. 6-7, 2016, pp. 595–613. https://doi.org/10.1177/1475472X16659388.

[35] Lorteau, M., Cléro, F., and Vuillot, F., "Analysis of noise radiation mechanisms in hot subsonic jet from a validated large eddy simulation solution," *Physics of Fluids*, Vol. 27, No. 7, 2015. https://doi.org/10.1063/1.4926792.

[36] Tyacke, J., Naqavi, I., Wang, Z.-N., Tucker, P., and Boehning, P., "Predictive Large Eddy Simulation for Jet Aeroacoustics–Current Approach and Industrial Application," *Journal of Turbomachinery*, Vol. 139, No. 8, 2017, pp. 081003–1–081003–13. https://doi.org/10.1115/1.4035662.

[37] Brès, G. A., Jordan, P., Jaunet, V., Le Rallic, M., Cavalieri, A. V. G., Towne, A., Lele, S. K., Colonius, T., and Schmidt, O. T., "Importance of the nozzle-exit boundary-layer state in subsonic turbulent jets," *Journal of Fluid Mechanics*, Vol. 851, 2018, p. 83–124. https://doi.org/10.1017/jfm.2018.476.

[38] Tyacke, J. C., Wang, Z.-N., and Tucker, P. G., "LES–RANS of Installed Ultra-High-Bypass-Ratio Coaxial Jet Aeroacoustics with Flight Stream," *AIAA Journal*, Vol. 57, No. 3, 2019, pp. 1215–1236. https://doi.org/10.2514/1.J057057.

[39] Wang, Z.-N., Proenca, A., Lawrence, J., Tucker, P. G., and Self, R., "Large-Eddy-Simulation Prediction of an Installed Jet Flow and Noise with Experimental Validation," *AIAA Journal*, Vol. 58, No. 6, 2020, pp. 2494–2503. https://doi.org/10.2514/1.J058921.

[40] Mockett, C., Fuchs, M., Kramer, F., Michel, U., Thiele, F., and Steger, M., "Further Development and Initial Validation of Innovative DES-Based Approaches for the Prediction of Jet Noise Installation Effects," *ASME Turbo Expo 2017: Turbomachinery Technical Conference and Exposition*, Charlotte, NC, 2017. https://doi.org/10.1115/GT2017-65253.

[41] Gand, F., Huet, M., Renaud, T., and Sartor, F., "ZDES of jets aeroacoustics: recent progress with unstructured grids and challenges," *AIAA AVIATION 2023 FORUM*, San Diego, CA, 2023.

[42] Uzun, A., and Hussaini, M. Y., "Simulation of Noise Generation in the Near-Nozzle Region of a Chevron Nozzle Jet," *AIAA Journal*, Vol. 47, No. 8, 2009, pp. 1793–1810. https://doi.org/10.2514/1.36659.

[43] Uzun, A., Bin, J., and Hussaini, M. Y., "High-Fidelity Numerical Simulation of a Chevron Nozzle Jet Flow," *International Journal of Aeroacoustics*, Vol. 10, No. 5-6, 2011, pp. 531–564. https://doi.org/10.1260/1475-472X.10.5-6.531.

[44] Bogey, C., Marsden, O., and Bailly, C., "Large-eddy simulation of the flow and acoustic fields of a Reynolds number 10^5 subsonic jet with tripped exit boundary layers," *Physics of Fluids*, Vol. 23, No. 3, 2011, pp. 035104–1–035104–20. https://doi.org/10.1063/1.3555634.

[45] Bogey, C., Marsden, O., and Bailly, C., "Influence of initial turbulence level on the flow and sound fields of a subsonic jet at a diameter-based Reynolds number of 10^5," *Journal of Fluid Mechanics*, Vol. 701, 2012, p. 352–385. https://doi.org/10.1017/jfm.2012.162.

[46] Bogey, C., and Marsden, O., "Simulations of Initially Highly Disturbed Jets with Experiment-Like Exit Boundary Layers," *AIAA Journal*, Vol. 54, No. 4, 2016, pp. 1299–1312. https://doi.org/10.2514/1.J054426.

[47] Paliath, U., and Premasuthan, S., "Large Eddy Simulation for Jet Installation Effects," *19th AIAA/CEAS Aeroacoustics Conference*, Berlin, Germany, 2013. https://doi.org/10.2514/6.2013-2137.

[48] Bodony, D. J., and Lele, S. K., "Current Status of Jet Noise Predictions Using Large-Eddy Simulation," *AIAA Journal*, Vol. 46, No. 2, 2008, pp. 364–380. https://doi.org/10.2514/1.24475.

[49] Brès, G. A., and Lele, S. K., "Modelling of jet noise: a perspective from large-eddy simulations," *Philosophical Transactions of the Royal Society A: Mathematical, Physical and Engineering Sciences*, Vol. 377, No. 2159, 2019, p. 20190081. https://doi.org/10.1098/rsta.2019.0081.

[50] Lyrintzis, A. S., and Coderoni, M., "Overview of the Use of Large-Eddy Simulations in Jet Aeroacoustics," *AIAA Journal*, Vol. 58, No. 4, 2020, pp. 1620–1638. https://doi.org/10.2514/1.J058498.

[51] Proença, A., Lawrence, J., and Self, R., "Experimental Investigation into the Turbulence Flow Field of In-Flight Round Jets," *AIAA Journal*, Vol. 58, No. 8, 2020, pp. 1–11. https://doi.org/10.2514/1.J059035.

[52] Mengaldo, G., Grazia, D. D., Witherden, F., Farrington, A., Vincent, P., Sherwin, S., and Peiro, J., "A Guide to the Implementation of Boundary Conditions in Compact High-Order Methods for Compressible Aerodynamics," *7th AIAA Theoretical Fluid Mechanics Conference*, Atlanta, GA, 2014. https://doi.org/10.2514/6.2014-2923.

[53] Roe, P., "Approximate Riemann solvers, parameter vectors, and difference schemes," *Journal of Computational Physics*, Vol. 43, No. 2, 1981, pp. 357–372. https://doi.org/10.1016/0021-9991(81)90128-5.

[54] Brown, P. N., and Saad, Y., "Convergence Theory of Nonlinear Newton–Krylov Algorithms," *SIAM Journal on Optimization*, Vol. 4, No. 2, 1994, pp. 297–330. https://doi.org/10.1137/0804017.

[55] Uranga, A., Persson, P.-O., Drela, M., and Peraire, J., "Implicit Large Eddy Simulation of transition to turbulence at low Reynolds numbers using a Discontinuous Galerkin method," *International Journal for Numerical Methods in Engineering*, Vol. 87, No. 1-5, 2011, pp. 232–261. https://doi.org/10.1002/nme.3036.

[56] Beck, A. D., Bolemann, T., Flad, D., Frank, H., Gassner, G. J., Hindenlang, F., and Munz, C.-D., "High-order discontinuous Galerkin spectral element methods for transitional and turbulent flow simulations," *International Journal for Numerical Methods in Fluids*, Vol. 76, No. 8, 2014, pp. 522–548. https://doi.org/10.1002/fld.3943.

[57] Carton de Wiart, C., Hillewaert, K., Bricteux, L., and Winckelmans, G., "Implicit LES of free and wall-bounded turbulent flows based on the discontinuous Galerkin/symmetric interior penalty method," *International Journal for Numerical Methods in Fluids*, Vol. 78, No. 6, 2015, pp. 335–354. https://doi.org/10.1002/fld.4021.

[58] Bergmann, M., Morsbach, C., and Franke, M., *Implicit LES of a Turbulent Channel Flow with High-Order Discontinuous Galerkin and Finite Volume Discretization*, Springer International Publishing, 2019, ERCOFTAC Series, Vol. 25, pp. 61–67. https://doi.org/10.1007/978-3-030-04915-7.

[59] Moura, R., Sherwin, S., and Peiró, J., "Linear dispersion–diffusion analysis and its application to under-resolved turbulence simulations using discontinuous Galerkin spectral/hp methods," *Journal of Computational Physics*, Vol. 298, 2015, pp. 695–710. https://doi.org/10.1016/j.jcp.2015.06.020.

[60] Moura, R., Mengaldo, G., Peiró, J., and Sherwin, S., "On the eddy-resolving capability of high-order discontinuous Galerkin approaches to implicit LES / under-resolved DNS of Euler turbulence," *Journal of Computational Physics*, Vol. 330, 2017, pp. 615–623. https://doi.org/10.1016/j.jcp.2016.10.056.

[61] Mengaldo, G., Moura, R., Giralda, B., Peiró, J., and Sherwin, S., "Spatial eigensolution analysis of discontinuous Galerkin schemes with practical insights for under-resolved computations and implicit LES," *Computers and Fluids*, Vol. 169, 2018, pp. 349–364. https://doi.org/10.1016/j.compfluid.2017.09.016.

[62] Farassat, F., "Derivation of Formulations 1 and 1A of Farassat," Technical Report NASA/TM-2007-214853, NASA, Hampton, VA, March 2007.

[63] Najafi-Yazidi, A., Brès, G. A., and Mongeau, L., "An Acoustic Analogy Formulation for Moving Sources in Uniformly Moving Media," *Proceedings of the Royal Society A, Mathematical, Physical and Engineering Sciences*, Vol. 467, No. 2125, 2011, pp. 144–165. https://doi.org/10.1098/rspa.2010.0172.

[64] Spalart, P. R., and Shur, M. L., "Variants of the Ffowcs Williams - Hawkings Equation and Their Coupling with Simulations of Hot Jets," *International Journal of Aeroacoustics*, Vol. 8, No. 5, 2009, pp. 477–491. https://doi.org/10.1260/147547209788549280.

[65] Mendez, S., Shoeybi, M., Lele, S. K., and Moin, P., "On the Use of the Ffowcs Williams-Hawkings Equation to Predict Far-Field Jet Noise from Large-Eddy Simulations," *International Journal of Aeroacoustics*, Vol. 12, No. 1-2, 2013, pp. 1–20. https://doi.org/10.1260/1475-472X.12.1-2.1.

[66] Rahier, G., Huet, M., and Prieur, J., "Additional terms for the use of Ffowcs Williams and Hawkings surface integrals in turbulent flows," *Computers and Fluids*, Vol. 120, 2015, pp. 158–172. https://doi.org/10.1016/j.compfluid.2015.07.014.

[67] Zhu, M., Pérez Arroyo, C., Fosso Pouangué, A., Sanjosé, M., and Moreau, S., "Isothermal and heated subsonic jet noise using large eddy simulations on unstructured grids," *Computers and Fluids*, Vol. 171, 2018, pp. 166–192. https://doi.org/10.1016/j.compfluid.2018.06.003.

[68] Welch, P., "The use of fast Fourier transform for the estimation of power spectra: A method based on time averaging over short, modified periodograms," *IEEE Transactions on Audio and Electroacoustics*, Vol. 15, No. 2, 1967, pp. 70–73. https://doi.org/10.1109/TAU.1967.1161901.

[69] Virtanen, P., Gommers, R., Oliphant, T. E., Haberland, M., Reddy, T., Cournapeau, D., Burovski, E., Peterson, P., Weckesser, W., Bright, J., van der Walt, S. J., Brett, M., Wilson, J., Millman, K. J., Mayorov, N., Nelson, A. R. J., Jones, E., Kern, R., Larson, E., Carey, C. J., Polat, İ., Feng, Y., Moore, E. W., VanderPlas, J., Laxalde, D., Perktold, J., Cimrman, R., Henriksen, I., Quintero, E. A., Harris, C. R., Archibald, A. M., Ribeiro, A. H., Pedregosa, F., van Mulbregt, P., and SciPy 1.0 Contributors, "SciPy 1.0: Fundamental Algorithms for Scientific Computing in Python," *Nature Methods*, Vol. 17, 2020, pp. 261–272. https://doi.org/10.1038/s41592-019-0686-2.

[70] Gand, F., and Huet, M., "On the generation of turbulent inflow for hybrid RANS/LES jet flow simulations," *Computers and Fluids*, Vol. 216, 2021. https://doi.org/10.1016/j.compfluid.2020.104816.

[71] Israeli, M., and Orszag, S. A., "Approximation of radiation boundary conditions," *Journal of Computational Physics*, Vol. 41, No. 1, 1981, pp. 115–135. https://doi.org/10.1016/0021-9991(81)90082-6.

[72] Choi, H., and Moin, P., "Grid-point requirements for large eddy simulation: Chapman's estimates revisited," *Physics of Fluids*, Vol. 24, No. 1, 2012, pp. 011702–1–011702–5. https://doi.org/10.1063/1.3676783.

[73] Jørgensen, F. E., "How to Measure Turbulence with Hot-Wire Anemometers - a Practical Guide," Technical Report, DANTEC Dynamics, Skovlunde, Denmark, 2002.

[74] Wang, Z.-N., Tyacke, J. C., and Tucker, P. G., "LES–RANS Study of Serrated Nozzle Jet Aeroacoustics for an Installed Ultra-High-Bypass-Ratio Aeroengine," *AIAA Journal*, Vol. 59, No. 10, 2021, pp. 4155–4165. https://doi.org/10.2514/1.J060447.

[75] Shur, M. L., Spalart, P. R., and Strelets, M. K., "Noise Prediction for Increasingly Complex Jets. Part II: Applications," *International Journal of Aeroacoustics*, Vol. 4, No. 3, 2005, pp. 247–266. https://doi.org/10.1260/1475472054771385.